



HAL
open science

Derivation and numerical resolution of 2D Shallow Water equations for multi-regime flows of Herschel-Bulkley fluids

David Michuri, Jerome Monnier, Mathieu Sellier

► **To cite this version:**

David Michuri, Jerome Monnier, Mathieu Sellier. Derivation and numerical resolution of 2D Shallow Water equations for multi-regime flows of Herschel-Bulkley fluids. 2024. hal-03968946v3

HAL Id: hal-03968946

<https://hal.science/hal-03968946v3>

Preprint submitted on 12 Apr 2024

HAL is a multi-disciplinary open access archive for the deposit and dissemination of scientific research documents, whether they are published or not. The documents may come from teaching and research institutions in France or abroad, or from public or private research centers.

L'archive ouverte pluridisciplinaire **HAL**, est destinée au dépôt et à la diffusion de documents scientifiques de niveau recherche, publiés ou non, émanant des établissements d'enseignement et de recherche français ou étrangers, des laboratoires publics ou privés.

Derivation and numerical resolution of 2D shallow water equations for multi-regime flows of Herschel-Bulkley fluids

David K. Muchiri^{a,b}, Jerome Monnier^b and Mathieu Sellier^a

^aDepartment of Mechanical Engineering, University of Canterbury, Christchurch 8140, New Zealand.

^bINSA & Institut de Mathématiques de Toulouse (IMT), 31400 Toulouse, France.

Correspondence author: jerome.monnier@insa-toulouse.fr

Abstract

This paper presents mathematical modelling and simulation of thin free-surface flows of viscoplastic fluids with a Herschel–Bulkley rheology over complex topographies with basal perturbations. Using the asymptotic expansion method, depth-averaged models (lubrication and shallow water type models) are derived for 3D (three-dimensional) multi-regime flows on non-flat inclined topographies with varying basal slipperiness conditions. Starting from the Navier–Stokes equations, two flow regimes corresponding to different balances between shear and pressure forces are presented. Flow models corresponding to these regimes are calculated as perturbations of the zeroth-order solutions. The classical reference models in the literature are recovered by considering their respective cases on a flat-inclined surface. In the second regime case, a pressure term is non-negligible. Mathematically, it leads to a corrective term to the classical regime equations. Flow solutions of the two regimes are compared; the difference appears in particular in the vicinity of sharp changes of slopes. Nonetheless, both regime models are compared with experiments and are found to be in good agreement. Furthermore, numerical examples are shown to illustrate the robustness of the present shallow water models to simulate viscoplastic flows in 3D and over an inclined topography with local perturbations in basal elevation and basal slipperiness. The derived models are adequate for direct (engineering and geophysical) applications to real-world flow problems presenting Herschel–Bulkley rheology like lava and mud flows.

Key words: Shallow water equations, lubrication, viscoplastic, basal slipperiness, free-surface flows, multi-regime flows.

1 Introduction

Free-surface flows of viscoplastic fluids are commonly encountered in nature (e.g., lava flows, debris flows, mudflows) [1–3] and in industrial settings (e.g., cosmetic creams, food pastes, paints, heavy oils) [3–5]. Mathematical modelling and simulation of these flows has a number of important geophysical and engineering applications [2, 6, 7]. One key application is the ability to predict the fluid flow path and run-out distances, for risk assessments and hazard management plans [7–9]. Reliable forecasting, however, calls for accurate modelling of the flow dynamics. For that reason, this paper aims at deriving a reliable model that can be used to simulate viscoplastic flows (like lava and mudflows) in a natural setting consisting of an irregular topography with varying basal slip distribution.

Viscoplastic materials are characterized by a yield stress threshold, beyond which they flow like fluids and below which they behave like rigid solids [4]. Flows of viscoplastic fluids have another complex behaviour

resulting from the formation of a plug-like (unyielded) region within the flow [2, 4]. Below this region is the sheared (yielded) zone; the interface between them is the yield surface. The possible coexistence and interaction of the two layers (regions) during the fluid evolution is still a paradox [2, 10–13]. This complex rheology makes it challenging to model viscoplastic flows. However, a number of rheological models have been developed in the past, and the most common are the Bingham and Herschel–Bulkley models which date back to the pioneering work of [14] and [15], respectively. This research work considers the Herschel–Bulkley law because of its ability to describe many complex fluid behaviors in a non-linear and history independent manner. In addition, this law has widely been used in the past to describe viscoplastic flows, see for instance [10, 16–21], and reference therein.

Apart from the complex rheology, geophysical flows of viscoplastic fluids have an additional complexity that arises from the free-surface evolution with time, the variation of basal conditions, and the rapidly unfolding complex topographies - which results in multi-regime flows (multiple regimes within the flow). Indeed, two different extreme regimes, fully sheared and sliding-like, can be observed within the flows. Different regimes within the flow usually originate from basal conditions that are non-uniform or potentially from variations of the mean-slope or basal elevation, see [22]. The conservation equations governing such flows, therefore, become rather more complex and difficult to solve numerically. However, geophysical flows are generally characterized by a small flow thickness compared to the flow extent, commonly referred to as the long-wave assumption, which allows to eliminate the vertical dimension by depth-integration [23, 24]. This yields the so-called thin-layer models (reduced models), such as the lubrication model and the shallow water model, that are easier to solve than the original complete Navier–Stokes equations.

Due to the increasing demand for fast and accurate viscoplastic models for hazard mitigation [7, 25, 26], we propose here to revisit and build on the derivations of shallow flow models in pursuit for one that can reproduce flows of viscoplastic fluids in a natural setting. Lubrication theory assumes that the flow is thin and slow [11, 24, 27]. This allows to reduce the conservation equations to a one-equation model (a scalar non-linear advection diffusion equation) governing the evolution of the fluid depth, see [10, 16, 17, 28–31] for derivation and applications. The Newtonian version of this approximation dates back to the work of Benney [32] prior to the Bingham (viscoplastic) one, which was pioneered by [27, 33]. However, the lubrication model fails to account for the effects of fluid inertial forces and the wet-dry front dynamics as the depth approaches zero, see [1, 13] and references therein. Some studies have also reported the singular behaviour of the model at high Reynolds number and/or when the linear stability threshold is exceeded [34–37].

On the other hand, the shallow water theory takes advantage of the long-wave assumption that allows to average the local mass and momentum conservation equations over the fluid depth. The resulting averaged quantities are then approximated by asymptotic analysis. This yields a two-equations model for the evolution of the local fluid depth and flow rate [22, 37]. One important advantage of this model over the lubrication model is that inertial terms are accounted for. The shallow water equations were first introduced by Barré de Saint-Venant for 1D hydraulic flows in 1887 [38]. Since then, there have been numerous derivation studies applicable to a variety of Newtonian flows e.g., [35, 39–42] and the flow of power-law fluids e.g., [22, 36, 37]. However, only a few studies have considered the case of viscoplastic flows, see [36, 43, 44] for Bingham and [45–47] for Herschel–Bulkley flows. Due to the complexity of calculating (and computing) these models, many of these derivations have been done based on a 2D (two-dimensional) flow problem which yields a 1D model (one-dimensional set of equations). It is of great importance to extend these derivations to 2D for practical applications in 3D.

Furthermore, despite the fact that many free-surface flows exhibit multiple flow regimes (ranging from

slow to fast, sliding to fully sheared, just to name a few) that arise from the variation of topography elevation and basal slip conditions, the existing derivations in the literature are mono-regime in the sense that they generally assume a flat configuration with non-changing basal conditions. However, there has been little effort to derive thin-layer models taking into account multi-regime flows. In particular, [48] derived unified thin-layer models for viscous fluids valid for fast and slow regimes, and [22] derived asymptotic thin-layer models (one equation and two equation type) for power-law fluids with varying basal boundary conditions corresponding to the multi-regimes aforementioned (including the flow regimes considered herein). This, however, has not yet been applied to viscoplastic flows. Incorporating basal properties (e.g., basal slipperiness) is important for accurate modelling of flow dynamics. Thus, the present article builds on the derivation of these models, in particular the shallow water equations partly presented in [46] and [22], and extends them to a 3D case that includes a topography elevation profile and a varying basal slip distribution on a non-flat inclined configuration with varying slip conditions at the bottom, therefore potentially presenting different flow regimes which are naturally defined as functions of dimensionless parameters. Note that multiple flow regimes (multi-regimes) can be encountered not only in geophysical flows but also in industrial settings, see e.g., [1, 4, 22].

In particular, the objective of the paper is to derive (and validate) a unified shallow water model for 3D multi-regime flows of Herschel Bulkley fluids over an inclined topography with perturbations in basal elevation and basal slipperiness. The outline of the paper is as follows. In Section 2, the flow configuration and the governing equations are defined. The primitive equations are non-dimensionalized, and the orders of magnitude of dimensionless parameters presented - from which two flow regimes are defined: Regime A, the basic/classical regime, and Regime B, the enriched one with a corrective term. In Section 3, the zeroth-order solutions corresponding to these flow regimes are presented. The one-equation model of lubrication type is re-derived therein. The derivation of the shallow water equations is presented in Section 4, an extension of the work of [22, 46]. Considering particular cases in the literature, classical shallow water models are recovered. In Section 5, the derived shallow water equations are validated with experiments, and the comparison of the two flow regimes discussed. Conclusions are drawn in Section 6.

2 Model formulation

We start by considering a 2D flow of a thin layer of a viscoplastic fluid on an inclined non-flat topography, as shown in Fig. 1, with x being the axis of the slope at an angle θ with the horizontal (of the reference plane) and z , the axis normal to the slope. The flow is driven by gravity $\underline{g} = (g\sin\theta, -g\cos\theta)$ and described by its velocity $\underline{u}(t, x, z) = (u(t, x, z), w(t, x, z))$, and the pressure field $p(t, x, z)$. The fluid is assumed to be incompressible with its density denoted by ρ . The fluid layer is of thickness $h(t, x, z) = (H(t, x, z) - b(x, z))$, where $H(t, x, z)$ is the fluid elevation and $b(x, z)$ the basal topography elevation.

For clarity, it is worthwhile noting that here we adopt a mean-slope coordinate system xz (with local variations of the topography), which can be related to the reference plane XZ (horizontal-vertical coordinate system) by the inclination θ , see Fig. 1. Another natural system of coordinates could be the Prandtl coordinate system as described in [22].

As usual, the flow dynamics are governed by the Navier–Stokes equations (conservation of mass and momentum, respectively):

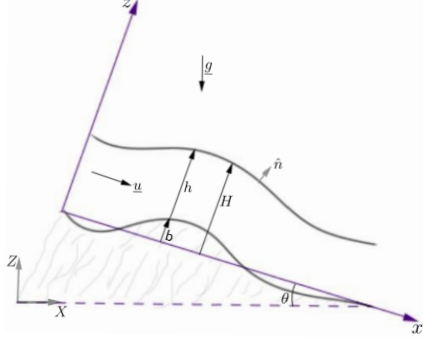


Figure 1: Flow configuration with a non-flat topography.

$$\begin{aligned}
\partial_x u + \partial_z w &= 0, \\
\rho(\partial_t u + u\partial_x u + w\partial_z u) &= -\partial_x p + \rho g \sin \theta + \partial_x \tau_{xx} + \partial_z \tau_{xz}, \\
\rho(\partial_t w + u\partial_x w + w\partial_z w) &= -\partial_z p - \rho g \cos \theta + \partial_x \tau_{zx} + \partial_z \tau_{zz},
\end{aligned} \tag{2.1}$$

where $\underline{\tau} = \begin{pmatrix} \tau_{xx} & \tau_{xz} \\ \tau_{zx} & \tau_{zz} \end{pmatrix}$ is the fluid stress tensor. The fluid rheology on the other hand, is described by the Herschel–Bulkley constitutive law which reads

$$\begin{cases} \tau_{ij} = \left(K \dot{\gamma}^{n-1} + \frac{\tau_c}{\dot{\gamma}} \right) \dot{\gamma}_{ij} & \text{for } \tau > \tau_c, \\ \dot{\gamma}_{ij} = 0 & \text{for } \tau \leq \tau_c, \end{cases} \tag{2.2}$$

where τ_{ij} and $\dot{\gamma}_{ij} = \partial_j u_i + \partial_i u_j$ are elements of the stress and strain rate tensors, $\tau = \sqrt{\frac{1}{2} \sum_{ij} \tau_{ij} \tau_{ij}}$ and $\dot{\gamma} = \sqrt{\frac{1}{2} \sum_{ij} \dot{\gamma}_{ij} \dot{\gamma}_{ij}}$ are the second invariant of the stress and strain rate tensors, $K > 0$ the consistency index, $n > 0$ the power-law index, and τ_c the yield stress, respectively.

It is worth noting that some geophysical flows like volcano lava, K is highly dependent on the fluid temperature T . In this case, K has simply to be given (or deduced by solving a thermal model).

Other fluid models can be recovered from the relation (2.2) depending on n and τ_c . For instance, when $n = 1$, the Herschel–Bulkley model reduces to a Bingham model where the consistency index K becomes the plastic viscosity η . When $n < 1$ the model reduces to a shear thinning fluid (pseudo-plastic) model in which the apparent viscosity increases the shear rate. When $n > 1$, a shear thickening (dilatant) fluid is obtained. When $n \neq 1$ and $\tau_c = 0$, a power-law fluid model is obtained. When $n = 1$ and $\tau_c = 0$, a Newtonian fluid model is recovered where K becomes the fluid viscosity.

The governing equations (2.1) - (2.2) are subject to the following boundary conditions at the bottom surface, $z = b$, and at the free-surface, $z = H$, respectively:

- The friction condition otherwise known as the power-law condition or the Weertman-type friction law (see e.g., [22, 49]), defined as

$$\begin{cases} \underline{u} \cdot \hat{t}_b &= -C |\underline{\tau} \cdot \hat{n}_b \cdot \hat{t}_b|^{\frac{1-n}{n}} \underline{\tau} \cdot \hat{n}_b \cdot \hat{t}_b, \\ \underline{u} \cdot \hat{n}_b &= 0, \end{cases} \quad (2.3)$$

where vectors \hat{t}_b and \hat{n}_b are the tangent and outward normal to the bottom, respectively, and C the basal slip coefficient. The negative sign allows C to be positive since \hat{n}_b is pointing outward. When $C = 0$, the no slip condition is recovered: $u = w = 0$.

- The kinematic condition: $\partial_t h + u \partial_x H = w$ and the no stress condition: $(\underline{\tau} - p \underline{I}) \cdot \hat{n} = 0$, where $\hat{n} = \frac{1}{\sqrt{1+(\partial_x H)^2}} \begin{pmatrix} \partial_x H \\ -1 \end{pmatrix}$ is the unit vector normal to the surface pointing outwards and \underline{I} the identity tensor. After a little algebra, the stress-free condition gives rise to two expressions: $\tau_{xz} = \frac{\partial_x H}{1-(\partial_x H)^2} (\tau_{xx} - \tau_{zz})$ and $p = \frac{1}{1-\partial_x H} (\tau_{zz} - (\partial_x H)^2 \tau_{xx})$.

Since the flow is incompressible, the mass conservation allows us to write the following equality: $\partial_x u = -\partial_z w \Leftrightarrow \tau_{xx} = -\tau_{zz}$.

2.1 Scaling and non-dimensionalization

To non-dimensionalize the primitive equations, L is set to be the characteristic length in the direction of the flow, \mathcal{H} the characteristic depth, U the scale of u and W the scale of w . By scaling and introducing dimensionless variables denoted by $'$ yields $x = Lx'$, $z = \mathcal{H}z'$, $t = \frac{L}{U}t'$, $b = \mathcal{H}b'$, $h = \mathcal{H}h'$, $H = \mathcal{H}H'$, $u = Uu'$ and $w = Ww'$. Assuming that the long-wave assumption holds, a geometric scaling parameter can be defined as $\epsilon = \frac{\mathcal{H}}{L} \ll 1$. The mass conservation equation allows us to naturally define $W = \frac{\mathcal{H}}{L}U$. Further, a hydrostatic pressure scale can be chosen as $p = \rho g \mathcal{H} \cos \theta p'$. Some standard scales are adopted for the fluid stresses:

$$(\tau_{xx}, \tau_{xz}, \tau_{zz}) = K \left(\frac{U}{\mathcal{H}} \right)^n (\epsilon \tau'_{xx}, \tau'_{xz}, \epsilon \tau'_{zz}).$$

The strain rate is scaled naturally as $\dot{\gamma} = \frac{U}{\mathcal{H}} \dot{\gamma}'$. Injecting these dimensionless variables into the primitive equations, some standard dimensionless groups can be defined: the Reynolds number, Froude number, and Bingham number, respectively:

$$Re = \frac{\rho U^{2-n} \mathcal{H}^n}{K}, \quad Fr = \frac{U}{\sqrt{g \mathcal{H} \cos \theta}}, \quad Bi = \frac{\tau_c}{K} \left(\frac{\mathcal{H}}{U} \right)^n.$$

Following the work of [22, 36, 37], some dimensionless parameters that occur naturally can be deduced:

$$(\beta, \alpha, \delta, \lambda) = \epsilon \left(Re, \gamma, \frac{1}{\gamma}, \frac{1}{\epsilon \gamma} \tan \theta \right),$$

where β , α , and δ are weight coefficients corresponding to the inertial, viscous, and pressure terms, respectively. The dimensionless parameter λ is the normalized gravity source term and $\gamma = \frac{Fr^2}{Re}$. For our

mathematical convenience we set $m = \frac{1}{n}$, where n is the power-law index. Dropping the apostrophe (') notation, the following dimensionless equations are obtained: the mass and momentum conservation equations, respectively:

$$\begin{aligned}\partial_x u + \partial_z w &= 0, \\ \beta(\partial_t u + u\partial_x u + w\partial_z u) &= -\delta\partial_x p + \lambda + \alpha\delta\partial_x\tau_{xx} + \partial_z\tau_{xz}, \\ \epsilon^2\beta(\partial_t w + u\partial_x w + w\partial_z w) &= -\delta(\partial_z p + 1) + \alpha\delta(\partial_x\tau_{zx} + \partial_z\tau_{zz}).\end{aligned}\tag{2.4}$$

and the rheological law:

$$\begin{cases} \tau_{xx} = -\tau_{zz} = 2\left(\frac{Bi}{\dot{\gamma}} + \dot{\gamma}^{n-1}\right)\partial_x u, \\ \tau_{xz} = \left(\frac{Bi}{\dot{\gamma}} + \dot{\gamma}^{n-1}\right)(\partial_z u + \alpha\delta\partial_x w) & \text{for } \tau > Bi, \\ \dot{\gamma}_{ij} = 0 & \text{for } \tau \leq Bi, \end{cases}\tag{2.5}$$

where $\dot{\gamma} = \sqrt{(\partial_z u + \alpha\delta\partial_x w)^2 + 4\alpha\delta(\partial_x u)^2}$, $\dot{\gamma}_{ij} = \begin{pmatrix} 2\epsilon\partial_x u & \partial_z u + \alpha\delta\partial_x w \\ \partial_z u + \alpha\delta\partial_x w & -2\epsilon\partial_x u \end{pmatrix}$ and $\tau = \sqrt{\tau_{xz}^2 + \alpha\delta\tau_{xx}^2}$.

At $z = b$, the scaled friction condition (see e.g [22]) writes

$$\begin{cases} u &= C \frac{|\tau_{xz}(1 - \alpha\delta\partial_x b^2) - 2\alpha\delta\tau_{xx}\partial_x b|^{m-1}}{(1 + \alpha\delta\partial_x b^2)^{m + \frac{1}{2}}} (\tau_{xz}(1 - \alpha\delta\partial_x b^2) - 2\alpha\delta\tau_{xx}\partial_x b), \\ w &= u\partial_x b. \end{cases}\tag{2.6}$$

At the free-surface $z = H$, the kinematic condition writes $\partial_t h + u\partial_x H - w = 0$ and the stress-free condition becomes

$$\tau_{xz} = \frac{\alpha\delta\partial_x H}{1 - \alpha\delta(\partial_x H)}(\tau_{xx} - \tau_{zz}), \quad p = \frac{\alpha}{(1 - \alpha\delta(\partial_x H)^2)}(\tau_{zz} - \alpha\delta(\partial_x H)^2\tau_{xx}).\tag{2.7}$$

2.2 Orders of magnitude of dimensionless parameters

To investigate the balance of different forces within the flow, field measurements of a real geophysical flow are scrutinized. In particular, measurements of volcano lava flows sourced from [50–54] are presented in Table 1 for analysis. The corresponding orders of magnitude of dimensionless parameters and weight coefficients are calculated as shown in Table 2. The average density of lava and inclination angle used for these calculations are $\rho = 2700\text{kgm}^{-3}$ and $\theta = 10^\circ$, respectively. From the order of magnitude in Table

	Composition	Temperature	Viscosity	Velocity
		T ($^\circ\text{C}$)	K (Pa s^n)	u (m/s)
Less viscous lava	Komatiite	1400 – 1600	10^0	10^1
Viscous lava (Intermediate)	Basalt	1200	10^2	10^{-1}
More viscous lava	Dacite/Rhyolite	900	10^7	10^{-2}

Table 1: Field measurements of three types of volcano lava flows, [50–54].

2, the following deductions can be made: the aspect ratio is small in the three regimes, which validates the long-wave assumption: $\epsilon \ll 1$. Previous studies have shown that this assumption is numerically valid up to $\epsilon \approx 0.3$, see e.g., [51, 55]. The dimensionless parameter α is small in the three regimes but relatively larger in the more viscous regime. The dimensionless parameter β is much smaller when lava is more viscous compared to other flow regimes; hence important when distinguishing the three regimes. On the other hand, δ is either

	ϵ	Re	Fr	β	α	δ	λ	$\frac{1}{\beta}$	$\frac{\delta}{\beta}$	$\frac{\alpha\delta}{\beta}$
Less viscous lava	10^{-5}	10^3	10^1	10^{-2}	10^{-7}	10^{-4}	10^1	10^1	10^3	10^{-9}
Viscous lava (Intermediate)	10^{-3}	10^0	10^{-2}	10^{-3}	10^{-7}	10^1	10^3	10^2	10^5	10^{-3}
More viscous lava	10^{-2}	10^{-5}	10^{-3}	10^{-7}	10^{-3}	10^{-1}	10^0	10^7	10^6	10^3

Table 2: Orders of magnitude of dimensionless parameters and weight coefficients.

small or of at most order 1, hence another important parameter to distinguish the regimes.

This implies that real flows are multi-regimes in (β, α, δ) . The gravity term λ is of at most order 3 and can be much higher on steep slopes. The Reynolds number Re and Froude number Fr for the less viscous lava (and the intermediate one) are much higher than those of the more viscous lava, which rules out consideration of the more viscous lava in this paper. Generally, komatiite and basaltic lava which are less viscous, are the most common lava flows on earth [51]. From this analysis, two regimes depending on β , α and δ can be defined:

- Regime A: with β small, α small, and δ small (less viscous lava).
- Regime B: with β small, α small, while $\delta = O(1)$ (intermediate viscous lava).

Considering these two regimes, the weight coefficient $\frac{\alpha\delta}{\beta}$ as seen in Table 3, is much smaller than other terms. Thus, it can be neglected; this will be recalled in the following sections. Furthermore, the asymptotic models corresponding to these two regimes will be derived in the next sections.

3 Zeroth-order field expressions

Firstly, we will start by deriving the steady-state uniform solutions (see Fig. 2 (a)) of the primitive equations, which are obtained by setting $h = \text{const}$, $b \equiv 0$ and $\alpha = \beta = \delta = 0$. This is equivalent to considering the zeroth-order approximations of Regime A: $\beta = \delta = \alpha = O(\epsilon)$. Next, we will derive the zeroth-order approximations of Regime B, that is, by considering $\beta = \alpha = O(\epsilon)$ and $\delta = O(1)$. For clarity, the calculations presented in this section are in 1D only, i.e., in space variables (x, z) .

3.1 Zeroth-order in Regime A sense

Considering $\beta = \delta = \alpha = O(\epsilon)$, the governing equations (2.4) - (2.7) simplify to

$$\begin{cases} \partial_z \tau_{xz} = -\lambda, \\ \partial_z p = -1. \end{cases} \quad (3.1)$$

$$\begin{cases} \tau_{xz} = Bi + (\partial_z u)^n & \text{if } \tau_{xz} > Bi, \\ \partial_z u = 0 & \text{if } \tau_{xz} \leq Bi. \end{cases} \quad (3.2)$$

The friction condition becomes $u = C|\tau_{xz}|^{m-1}\tau_{xz}$, $w = 0$, from which a non-slip condition is recovered when the slip coefficient $C = 0$ and a pure slip when $C \rightarrow \infty$. The free-surface conditions become $\tau_{xz} = 0$, and

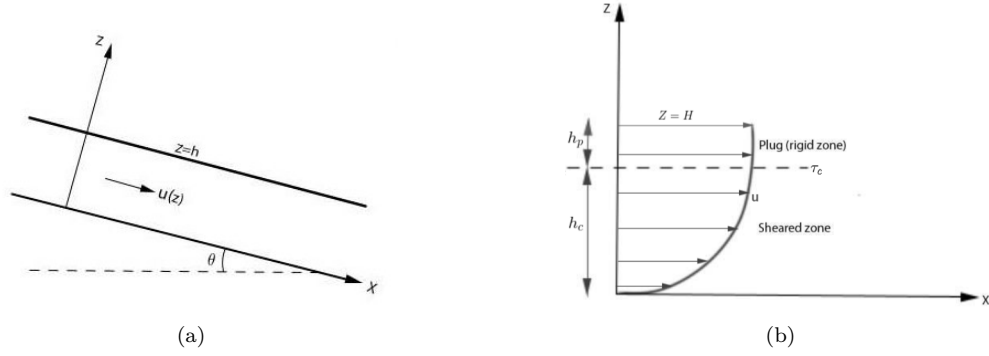


Figure 2: Sketch of (a) a steady uniform flow configuration and (b) the velocity profile showing the plug and sheared zones in Herschel–Bulkley flows

$p = 0$. Recall that $Bi = \frac{\tau_c}{K} \left(\frac{H}{U}\right)^n$.

Solving Eq. (3.1), a hydrostatic pressure and shear stress linear in z are obtained:

$$p = h - z, \quad \tau_{xz} = \lambda(h - z). \quad (3.3)$$

Consequently, the friction condition reduces to $u = C(\lambda h)^m$ and $w = 0$. Near the free-surface as $z \rightarrow h$, the shear stress component $\tau_{xz} \rightarrow 0$, which implies the existence of a plug-like flow near the free-surface of thickness h_p (see Fig. 2 (b)) such that

$$h_p = \frac{Bi}{\lambda}. \quad (3.4)$$

Next, solving for the stream-wise velocity using Eqs. (3.2) - (3.4) yields

$$u(z) = \lambda^m \begin{cases} \frac{1}{m+1} h_c^{m+1} \left[1 - \left(1 - \frac{z-b}{h_c}\right)^{m+1} \right] + Ch^m, & \text{for } z < h_c \\ \frac{1}{m+1} h_c^{m+1} + Ch^m, & \text{for } z \geq h_c \end{cases} \quad (3.5)$$

where, $h_c = \max(0, h - h_p)$ represents the thickness of the sheared zone below the plug. The flow rate can also be obtained by $q = h\bar{u} = \int_b^H u dz$ where \bar{u} is the mean velocity:

$$q = \lambda^m \left[h_c^{m+1} \left(\frac{1}{m+1} h_p + \frac{1}{m+2} h_c \right) + Ch^{m+1} \right]. \quad (3.6)$$

For the Newtonian case where $Bi = 0$, $m = 1$, and taking $C = 0$, the plug is absent i.e. $h_c = h$. This results in a Poiseuille-like velocity profile: $u(z) = \frac{1}{2}\lambda h^2 \left[1 - \left(1 - \frac{z}{h}\right)^2 \right]$, and the average velocity \bar{u} in terms of thickness h becomes $\bar{u} = \frac{1}{3}\lambda h^2$.

The zeroth-order solutions are important as they show the main properties of solutions and serve as reference solutions for other flow regimes. In particular, the asymptotic fields of other flow regimes considered in the following sections are perturbations of these reference solutions.

3.2 Zeroth-order in Regime B sense

Regime B approximations are obtained by considering the 0^{th} order terms in (α, β) , while $\delta = O(1)$.

Consequently, Eqs. (2.4) - (2.5) reduce to the following system:

$$\partial_x u + \partial_z w = 0, \quad (3.7)$$

$$\begin{cases} \partial_z \tau_{xz} = \delta \partial_x p - \lambda, \\ \partial_z p = -1, \end{cases} \quad (3.8)$$

and the constitutive law becomes

$$\begin{cases} \tau_{xx} = -\tau_{zz} = 2 \left(\frac{Bi}{\partial_z u} + (\partial_z u)^{n-1} \right) \partial_x u, & \tau_{xz} = Bi + (\partial_z u)^n & \text{for } \tau_{xz} > Bi, \\ \partial_z u = 0 & & \text{for } \tau_{xz} \leq Bi. \end{cases} \quad (3.9)$$

The boundary conditions, on the other hand, reduce to $u = C|\tau_{xz}|^{m-1}\tau_{xz}$, $w = u\partial_x b$ at $z = b$ and $\partial_t h + u\partial_x H = w$, $\tau_{xz} = 0$, $p = 0$ at $z = H$. By integration, Eq. (3.8) yields a hydrostatic pressure $p = H(x, t) - z$ and an expression for the shear stress

$$\tau_{xz} = (\lambda - \delta \partial_x H)(H - z). \quad (3.10)$$

which represents a balance between the shear stress and the hydrostatic pressure gradient. The modulus of Eq. (3.10) can be obtained as:

$$|\tau_{xz}| = |\lambda - \delta \partial_x H|(H - z). \quad (3.11)$$

which implies that for a vanishing slope angle in the gravity term λ , the sign of the shear stress τ_{xz} remains the same as the sign of the local slope of the free-surface. Eqs. (3.3) and (3.10) suggest to introduce the variable Λ as in Boutounet et al. [2]:

$$\Lambda = \begin{cases} \lambda & \text{for regime A,} \\ \lambda - \delta \partial_x H & \text{for regime B,} \end{cases} \quad (3.12)$$

which allows to write unified expressions representing the two regimes.

Further, as seen previously in the case of Regime A approximations, Eq. (3.10) shows that the evolution of the shear stress is linear in depth. As $z \rightarrow H$, the shear stress component $\tau_{xz} \rightarrow 0$, indicating the existence of an unyielded zone near the free-surface (see Fig. 2 (b)) whose thickness now writes

$$h_p = \frac{Bi}{\Lambda}. \quad (3.13)$$

This thickness, however, is not constant; it varies with the thickness gradient of the free-surface, which implies the existence of some elongational deformation in the plug. This contradicts the validity of zero-order approximations. To resolve this contradiction, a concept of pseudo-plug has been introduced, see [10, 11, 36], where the plug is made weakly sheared under the influence of normal stresses.

Furthermore, by integrating the constitutive law (3.9) and using the fact that $H = (h_p + h_c + b)$, Eqs.

(3.9) - (3.13) enable to obtain the velocity field expression:

$$u(z) = \Lambda|\Lambda|^{m-1} \begin{cases} \left[\frac{1}{m+1} h_c^{m+1} \left(1 - \left(1 - \frac{z-b}{h_c} \right)^{m+1} \right) + Ch^m \right] & \text{if } z < h_c + b, \\ \left[\frac{1}{m+1} h_c^{m+1} + Ch^m \right] & \text{if } z \geq h_c + b, \end{cases} \quad (3.14)$$

which is locally identical to that of the Regime A solution, a perturbation of the reference flow. Also, by integration, an expression for the discharge $q = h\bar{u}$ can be obtained:

$$q = \Lambda|\Lambda|^{m-1} \left[h_c^{m+1} \left(\frac{1}{m+1} h_p + \frac{1}{m+2} h_c \right) + Ch^{m+1} \right] \quad (3.15)$$

3.3 On the lubrication-type flow model

The so-called lubrication flow model is derived from the discharge expression and the depth-integrated mass equation. The latter is obtained by integrating Eq. (3.7) from $z = b$ to $z = H$, which, after applying the Leibniz integral rule and the boundary conditions, reads $\frac{\partial h}{\partial t} + \frac{\partial q}{\partial x} = 0$. In the Regime B case, the lubrication type model (also called one-equation model) reads

$$\frac{\partial h}{\partial t} + \frac{\partial}{\partial x} \left(\Lambda|\Lambda|^{m-1} \left(h_c^{m+1} \left(\frac{1}{m+1} h_p + \frac{1}{m+2} h_c \right) + Ch^{m+1} \right) \right) = 0.$$

By setting $Bi = 0$ and $m = 1$, a simplified Newtonian model of Benney's type with no surface tension term is recovered (see [24, 32]).

The main advantage of the lubrication-type model is that since it is a scalar non-linear equation, it is computationally less expensive to solve. However, this model can fail to capture important flow details, like the effects of inertial terms, which are neglected at order zero. The model is also not consistent with the wet-dry front dynamics as $h \rightarrow 0$, see e.g., [24] and references therein. In addition, it can present singularities in finite time when the linear stability threshold is exceeded, see [34–36] and references therein. The solution to some of these issues is to consider the two-equations model derived in the next section.

4 Shallow water type models

Assuming the long-wave assumption ($\epsilon \ll 1$) holds, the shallow water equations are obtained by depth integration of the Cauchy mass and momentum equations (2.4). For the sake of clarity, the derivations are first done in 2D (to obtain a 1D model), then extended to 3D (to obtain a 2D model).

4.1 The 1D model

The first model equation is the integrated mass conservation: $\frac{\partial h}{\partial t} + \frac{\partial q}{\partial x} = 0$. Next, to obtain the second equation, the momentum equation is integrated over the fluid depth, which, after applying the Leibniz integral rule together with the boundary conditions at order 1 in (α, δ) , give

$$\beta \left(\frac{\partial}{\partial t} \int_b^H u dz + \frac{\partial}{\partial x} \int_b^H u^2 dz \right) + \delta \frac{\partial}{\partial x} \int_b^H p dz = \epsilon^2 \frac{\partial}{\partial x} \int_b^H \tau_{xx} dz + \lambda h - \tau_{xz}|_{z=b} - (\delta p|_{z=b} - \epsilon^2 \tau_{xx}|_{z=b}) \frac{\partial b}{\partial x}.$$

After a few arrangements, taking $q = h\bar{u} = \int_b^H u dz$ and the shear stress at the base as $\sigma_{xz}|_{z=b} = \tau_b$, the second equation in variables (h, q) is obtained as

$$\frac{\partial h\bar{u}}{\partial t} + \frac{\partial}{\partial x} \int_b^H u^2 dz - \frac{\alpha\delta}{\beta} \frac{\partial}{\partial x} \int_b^H \tau_{xx} dz + \frac{\delta}{\beta} \frac{\partial}{\partial x} \int_b^H p dz + \frac{\delta}{\beta} (p|_{z=b} - \alpha\tau_{xx}|_{z=b}) \frac{\partial b}{\partial x} = \frac{1}{\beta} (\lambda h - \tau_b). \quad (4.1)$$

To close this model, the averaged quantities: $\int_b^H u^2$, $\int_b^H \tau_{xx}$, and $\int_b^H p$, need to be related to the state variables h and \bar{u} , see [22, 36, 37, 46]. This is done by asymptotic approximations. Due to the complex flow behaviour of geophysical viscoplastic flows (like lava, muds, etc), the zeroth-order approximations are usually assumed to be sufficient to close the model. The one-order approximations are more consistent therefore important for perfectly reproducible flows (like flows of perfect fluids). However, for geophysical flows, they may be too complex to set up, costly to compute, and unnecessary owing to other uncertainties. For that reason, the following approximations are developed at order zero, following the calculations presented in [22, 46]:

- i. Assuming $u \approx \bar{u}$, the averaged quantity $\int_b^H u^2 dz$ can be approximated as $\int_b^H u^2 dz \simeq \int_b^H u^{(0)2} dz \approx \frac{q^2}{h} +$ "the corrective term", where the corrective term is adopted from [22] as $\frac{\Lambda^{2m} h^{2m+3}}{(2m+3)(m+2)^2}$. It is important to note that the corrective term vanishes as Λ vanishes.
- ii. The averaged pressure term is approximated as $\int_b^H p dz \simeq \int_b^H p^{(0)} dz = \frac{h^2}{2}$.
- iii. The terms of order $\frac{\alpha\delta}{\beta}$ are negligibly small, as seen previously in Table 3, hence can be dropped.
- iv. The basal shear stress τ_b can be approximated from Eqs. (3.10) and (3.13) as

$$\tau_b^{(0)} = \tau_{xz}^{(0)}|_{z=b} = \Lambda h = \Lambda (h_p + h_c) \quad (4.2)$$

which, if inserted into the momentum equation (4.1) the source terms degenerate. This implies that the zeroth-order approximation (4.2) is not sufficient to close the model in a consistent way, hence not adequate to describe non-uniform flows. A solution to this issue is to express $\tau_b^{(0)}$ in terms of $q = h\bar{u}$ following [22, 46]. Consequently, Eq. (3.15) and Eq. (4.2) allow to write

$$\tau_b^{(0)} = |\Lambda|^{1-m} (h_p + h_c) \frac{q}{D(h)}. \quad (4.3)$$

where the denominator $D(h)$ is given by $D(h) = h_c^{m+1} \left(\frac{1}{m+1} h_p + \frac{1}{m+2} h_c \right) + C h^{m+1}$.

Applying the above approximations into Eq. (4.1) (dropping the zeroth-order notation), the momentum equation (4.1) writes

$$\frac{\partial q}{\partial t} + \frac{\partial}{\partial x} \left(\frac{q^2}{h} + \frac{\Lambda^{2m} h^{2m+3}}{(2m+3)(m+2)^2} \right) + \frac{\delta}{\beta} h \frac{\partial H}{\partial x} = \frac{1}{\beta} (\lambda h - \tau_b), \quad (4.4)$$

with the basal shear stress given by Eq. 4.3.

Comparison with models in the literature for simpler rheology cases

Considering the Newtonian case ($Bi = 0$, $m = 1$, and taking $C = 0$), Eq. (4.3) reduces to $\tau_b = \frac{3\bar{u}}{h}$. This recovers the multi-regime two-equations model for a Newtonian fluid presented in [22]:

$$\frac{\partial h}{\partial t} + \frac{\partial q}{\partial x} = 0, \quad \frac{\partial q}{\partial t} + \frac{\partial}{\partial x} \left(\frac{q^2}{h} + \frac{\delta}{2\beta} h^2 + \frac{\Lambda^2 h^5}{45} \right) = \frac{1}{\beta} \left(\lambda h - \frac{3q}{h^2} \right). \quad (4.5)$$

In the mono-regime version (Regime B), the Bingham fluid case ($Bi > 0$ and $m = 1$) is recovered as in [36]. Similarly, by setting $Bi = 0$ and $m \neq 1$, the shallow water model for power-law fluids presented in [36, 37] is recovered.

4.2 The 2D model

Here, we extend the calculations to 2D i.e., in variables (x, y, z) . To do so, the shallow water system is derived by averaging the 3D incompressible Navier–Stokes equations presented below over the fluid depth, taking into account the asymptotic approximations obtained in the previous subsection.

The primitive equations

For the purpose of derivations, a configuration in which either x or y is the axis of the slope at an angle θ with z being the axis normal to the slope is considered.

$$\begin{aligned} \beta(\partial_t u + u\partial_x u + v\partial_y u + w\partial_z u) &= -\delta\partial_x p + \lambda_x + \alpha\delta(\partial_x \tau_{xx} + \partial_y \tau_{xy}) + \partial_z \tau_{xz}, \\ \beta(\partial_t v + u\partial_x v + v\partial_y v + w\partial_z v) &= -\delta\partial_y p + \lambda_y + \alpha\delta(\partial_x \tau_{yx} + \partial_y \tau_{yy}) + \partial_z \tau_{yz}, \\ \epsilon^2 \beta(\partial_t w + u\partial_x w + v\partial_y w + w\partial_z w) &= -\delta(\partial_z p + 1) + \alpha\delta(\partial_x \tau_{zx} + \partial_y \tau_{zy} + \partial_z \tau_{zz}). \end{aligned} \quad (4.6)$$

Considering the 0^{th} order terms in ϵ and assuming $\beta = \alpha = O(\epsilon)$ (equivalent to the Regime B case), the governing equations reduce to the following system of equations: the continuity equation: $\partial_x u + \partial_y v + \partial_z w = 0$, the momentum balance equation:

$$\begin{cases} \partial_z \tau_{xz} = \delta\partial_x p - \lambda_x, \\ \partial_z \tau_{yz} = \delta\partial_y p - \lambda_y, \\ \partial_z p = -1. \end{cases} \quad (4.7)$$

and the Herschel–Bulkley rheology law introduced in Section 2:

$$\begin{cases} \tau_{xz} = \left(\frac{Bi}{\dot{\gamma}} + \dot{\gamma}^{n-1} \right) \partial_z u, \quad \tau_{yz} = \left(\frac{Bi}{\dot{\gamma}} + \dot{\gamma}^{n-1} \right) \partial_z v & \text{if } \tau > Bi, \\ \dot{\gamma}_{ij} = 0 & \text{if } \tau \leq Bi, \end{cases} \quad (4.8)$$

where the deformation tensor norm: $\dot{\gamma} = \sqrt{(\partial_z u)^2 + (\partial_z v)^2}$ and the stress norm:

$$\tau = \sqrt{\tau_{xz}^2 + \tau_{yz}^2}. \quad (4.9)$$

The system is completed by boundary conditions at the bottom surface: the friction condition which reduces to $u = C|\tau_{xz}|^{m-1}\tau_{xz}$, $v = C|\tau_{yz}|^{m-1}\tau_{yz}$, $w = u\partial_x b + v\partial_y b$, and at the free-surface we have the non-stress conditions: $\tau_{xz} = \tau_{yz} = 0$, $p = 0$, and the kinematic condition: $\partial_t h + u\partial_x H + v\partial_y H = w$.

Field equations

Straightforward integration of Eq. (4.7) yields a hydrostatic pressure $p = H(x, y, t) - z$ and the following expressions for the shear stresses

$$\tau_{xz} = \Lambda_x(H - z), \quad \tau_{yz} = \Lambda_y(H - z), \quad (4.10)$$

where, if x is considered as the axis of the slope, y as the spanwise coordinate, and z the normal axis to the slope, Λ defined in Section 3.2 writes

$$\bar{\Lambda} = \lambda \binom{1}{0} \text{ for regime A, } \quad \bar{\Lambda} = \lambda \binom{1}{0} - \delta \binom{\partial_x H}{\partial_y H} \text{ for regime B.} \quad (4.11)$$

Otherwise, when considering a general case in which the axis of the slope is either x or y , the gravity term can be written as

$$\bar{\Lambda} = \lambda \binom{1}{1} \text{ for regime A, } \quad \bar{\Lambda} = \lambda \binom{1}{1} - \delta \binom{\partial_x H}{\partial_y H} \text{ for regime B.} \quad (4.12)$$

Eq. (4.9) can now be written in terms of Λ as

$$\tau = \sqrt{(\Lambda_x^2 + \Lambda_y^2)}(H - z). \quad (4.13)$$

On the yield surface: $\tau = Bi$ and $h = h_c$, thus the thickness of the sheared zone is obtained as

$$h_c = h - \frac{Bi}{\|\Lambda\|} \quad \text{for } \tau > Bi, \quad (4.14)$$

which in general, writes: $h_c = \max(0, h - h_p)$, where the plug thickness $h_p = \frac{Bi}{\|\Lambda\|}$ and $\|\Lambda\| = \sqrt{(\Lambda_x^2 + \Lambda_y^2)}$. Next, from the rheology law (4.8), τ can be written as

$$\tau = \sqrt{\tau_{xz}^2 + \tau_{yz}^2} = Bi + \dot{\gamma}^n. \quad (4.15)$$

Note that Eq. (4.13) and Eq. (4.15) are equivalent, which after some algebra translate to

$$\partial_z u = \Lambda_x (h_c + b - z)^{\frac{1}{n}}, \quad \partial_z v = \Lambda_y (h_c + b - z)^{\frac{1}{n}} \quad (4.16)$$

in the x - and y -directions, respectively. Integrating these expressions and applying the friction condition, the velocity distribution in the x - and y -directions, respectively, is obtained:

$$u(z) = \Lambda_x |\Lambda_x|^{m-1} \begin{cases} \left[\frac{1}{m+1} \left(h_c^{m+1} - (h_c - z - b)^{m+1} \right) + Ch^m \right] & \text{if } z < h_c, \\ \left[\frac{1}{m+1} h_c^{m+1} + Ch^m \right] & \text{if } z \geq h_c. \end{cases} \quad (4.17)$$

$$v(z) = \Lambda_y |\Lambda_y|^{m-1} \begin{cases} \left[\frac{1}{m+1} \left(h_c^{m+1} - (h_c - z - b)^{m+1} \right) + Ch^m \right] & \text{if } z < h_c, \\ \left[\frac{1}{m+1} h_c^{m+1} + Ch^m \right] & \text{if } z \geq h_c. \end{cases}$$

The flow rate in both directions is finally obtained as $q_x = h\bar{u} = \int_b^H u dz$ and $q_y = h\bar{v} = \int_b^H v dz$, respectively,

$$\begin{aligned}
q_x &= \Lambda_x |\Lambda_x|^{m-1} \left[h_c^{m+1} \left(\frac{1}{m+1} h_p + \frac{1}{m+2} h_c \right) + Ch^{m+1} \right], \\
q_y &= \Lambda_y |\Lambda_y|^{m-1} \left[h_c^{m+1} \left(\frac{1}{m+1} h_p + \frac{1}{m+2} h_c \right) + Ch^{m+1} \right].
\end{aligned} \tag{4.18}$$

The two-equations model

The first equation of the SW model reads in 2D as $\frac{\partial h}{\partial t} + \frac{\partial q_x}{\partial x} + \frac{\partial q_y}{\partial y} = 0$. Following the approach presented earlier for the 1D case, the x- and y-momentum equations are integrated over the fluid depth, applying Leibniz integral rule and the boundary conditions to obtain the x-component:

$$\begin{aligned}
\frac{\partial h \bar{u}}{\partial t} + \frac{\partial}{\partial x} \int_b^H u^2 dz + \frac{\partial}{\partial y} \int_b^H u v dz - \frac{\alpha \delta}{\beta} \left(\frac{\partial}{\partial x} \int_b^H \tau_{xx} dz + \frac{\partial}{\partial y} \int_b^H \tau_{xy} dz + \tau_{xy}|_{z=b} \frac{\partial b}{\partial y} - \tau_{xy}|_{z=H} \frac{\partial H}{\partial y} \right) \\
+ \frac{\delta}{\beta} \frac{\partial}{\partial x} \int_b^H p dz + \frac{\delta}{\beta} (p|_{z=b} - \alpha \tau_{xx}|_{z=b}) \frac{\partial b}{\partial x} = \frac{1}{\beta} (\lambda_x h - \tau_{b_x}),
\end{aligned}$$

and the y-component:

$$\begin{aligned}
\frac{\partial h \bar{v}}{\partial t} + \frac{\partial}{\partial x} \int_b^H u v dz + \frac{\partial}{\partial y} \int_b^H v^2 dz - \frac{\alpha \delta}{\beta} \left(\frac{\partial}{\partial x} \int_b^H \tau_{xy} dz + \frac{\partial}{\partial y} \int_b^H \tau_{yy} dz + \tau_{xy}|_{z=b} \frac{\partial b}{\partial x} - \tau_{xy}|_{z=H} \frac{\partial H}{\partial x} \right) \\
+ \frac{\delta}{\beta} \frac{\partial}{\partial y} \int_b^H p dz + \frac{\delta}{\beta} (p|_{z=b} - \alpha \tau_{yy}|_{z=b}) \frac{\partial b}{\partial y} = \frac{1}{\beta} (\lambda_y h - \tau_{b_y}).
\end{aligned}$$

Considering the zeroth-order approximations defined at the beginning of this section, the two-equations model in 2D reads

$$\begin{aligned}
\frac{\partial h}{\partial t} + \frac{\partial h \bar{u}}{\partial x} + \frac{\partial h \bar{v}}{\partial y} &= 0, \\
\frac{\partial h \bar{u}}{\partial t} + \frac{\partial}{\partial x} \left(h \bar{u}^2 + \frac{\delta}{2\beta} h^2 + C_m \Lambda_x^{2m} h^{2m+3} \right) + \frac{\partial}{\partial y} (h \bar{u} \bar{v} + C_m \Lambda_y^{2m} h^{2m+3}) &= \frac{1}{\beta} \left(\lambda_x h - \delta h \frac{\partial b}{\partial x} - \tau_{b_x} \right), \\
\frac{\partial h \bar{v}}{\partial t} + \frac{\partial}{\partial x} (h \bar{u} \bar{v} + C_m \Lambda_x^{2m} h^{2m+3}) + \frac{\partial}{\partial y} \left(h \bar{v}^2 + \frac{\delta}{2\beta} h^2 + C_m \Lambda_y^{2m} h^{2m+3} \right) &= \frac{1}{\beta} \left(\lambda_y h - \delta h \frac{\partial b}{\partial y} - \tau_{b_y} \right),
\end{aligned} \tag{4.19}$$

with the basal shear stress components approximated at order zero from Eq. (4.10), which after substituting Eq. (4.18) for Λ in both directions, yield

$$\tau_{b_x} = |\Lambda_x|^{1-m} \left(\frac{Bi}{|\Lambda|} + h_c \right) \frac{q_x}{D(h)}, \quad \tau_{b_y} = |\Lambda_y|^{1-m} \left(\frac{Bi}{|\Lambda|} + h_c \right) \frac{q_y}{D(h)}, \tag{4.20}$$

where the denominator $D(h) = h_c^{m+1} \left(\frac{1}{m+1} h - \frac{1}{(m+1)(m+2)} h_c \right) + Ch^{m+1}$, see Eq. 3.15, and $C_m = \frac{1}{(2m+3)(m+2)^2}$. Recall that $(q_x, q_y) = h(\bar{u}, \bar{v})$.

In dimensional form the two-equations model in 2D writes

$$\begin{aligned}
& \frac{\partial h}{\partial t} + \frac{\partial q_x}{\partial x} + \frac{\partial q_y}{\partial y} = 0, \\
& \frac{\partial q_x}{\partial t} + \frac{\partial}{\partial x} \left(\frac{q_x^2}{h} + \frac{1}{2}gh^2\cos\theta + C_m\Lambda_x^{2m}h^{2m+3} \right) + \frac{\partial}{\partial y} \left(\frac{q_xq_y}{h} + C_m\Lambda_y^{2m}h^{2m+3} \right) = gh\cos\theta \left(\tan\theta - \frac{\partial b}{\partial x} \right) - \frac{1}{\rho}\tau_{b_x}, \\
& \frac{\partial q_y}{\partial t} + \frac{\partial}{\partial x} \left(\frac{q_xq_y}{h} + C_m\Lambda_x^{2m}h^{2m+3} \right) + \frac{\partial}{\partial y} \left(\frac{q_y^2}{h} + \frac{1}{2}gh^2\cos\theta + C_m\Lambda_y^{2m}h^{2m+3} \right) = hg\cos\theta \left(\tan\theta - \frac{\partial b}{\partial y} \right) - \frac{1}{\rho}\tau_{b_y},
\end{aligned} \tag{4.21}$$

where $\bar{\Lambda} = \frac{\rho g}{K}\bar{S}_\theta$, with $\bar{S}_\theta = \sin\theta \binom{1}{0}$ for Regime A, or $\bar{S}_\theta = \sin\theta \binom{1}{0} - \cos\theta \binom{\partial_x H}{\partial_y H}$ for Regime B.

The basal shear stress expressed in function of τ_c reads as

$$\boldsymbol{\tau}_b = \begin{bmatrix} \tau_{b_x} \\ \tau_{b_y} \end{bmatrix} = \begin{bmatrix} K \left(\frac{K}{\rho g |S_{\theta_x}|} \right)^{m-1} \left(\frac{\tau_c}{\rho g |S_\theta|} + h_c \right) \frac{q_x}{D(h)} \\ K \left(\frac{K}{\rho g |S_{\theta_y}|} \right)^{m-1} \left(\frac{\tau_c}{\rho g |S_\theta|} + h_c \right) \frac{q_y}{D(h)} \end{bmatrix}, \tag{4.22}$$

where, as presented previously, the sheared thickness $h_c = \max(0, h - h_p)$, the plug thickness $h_p = \frac{\tau_c}{\rho g |S_\theta|}$ and finally $\left(\frac{\tau_c}{\rho g |S_\theta|} + h_c \right) = h$.

It is worth noting that Regime A equations are not valid for a vanishing mean-slope (horizontal case), since the solution blows up when $\theta = S_\theta = 0$. Further, by setting $\tau_c = 0$, $m = 1$ and $\theta = 0$ (for Regime B), the shallow water equations for Newtonian flows (mono-regime version) are recovered.

On the global geometry assumption and coordinate system

In the present study, all derivations have been presented in the mean-slope coordinate system with local topography variations about the mean-position, see Fig. 1. This geometry is the most classical, straightforward, and reasonable in a large number of applications. However, this mean-slope geometry assumption can be limiting, especially for large variations of mean inclinations. To overcome this, [22] uses the Prandtl coordinate system, which allows the variation of the topography without the existence of a fixed mean-slope.

Moreover, when using the mean-slope geometry as in the present derivations, it is numerically observed that the momentum gravity source term $gh\cos\theta\tan\theta$ of Eq. (4.21) overestimates dam-break flow solutions for relatively large inclinations. However, based on the facts that dam-break flows are mainly driven by the streamwise pressure gradient $\left(\frac{\partial h}{\partial x}, \frac{\partial h}{\partial y} \right)$, and that the front zone of the current is usually determined by the balance between the gravitational acceleration $g \left(\frac{\partial h}{\partial x}, \frac{\partial h}{\partial y} \right)$ and the basal friction (τ_{b_x}, τ_{b_y}) [56, 57], a possible solution to this issue consists to further express the gravity source in terms of the height gradient. Consequently, based on the coordinate systems defined in Fig. 1 (taking $b \equiv 0$), we can consider that $gh\cos\theta\tan\theta\mathbf{I} \simeq -gh\sec\theta \left(\frac{\partial h}{\partial x}, \frac{\partial h}{\partial y} \right)$ with $\sec\theta = (\cos\theta)^{-1}$. If x - is considered as the axis of the slope, this reads $gh\cos\theta\tan\theta\mathbf{I} \simeq -gh\sec\theta \left(\frac{\partial h}{\partial x}, 0 \right)$. This is applied to dam-break flow simulations in the following section.

5 Numerical results

This section presents the computed results of a few cases considered using the shallow water type system (4.21). To start with, a mesh convergence test is performed; thereafter, numerical results are compared with experimental results for validation. The comparison of the two regime models within a steady-state flow and an unsteady (dam-break) one is investigated afterwards. Further results are shown for 3D applications. Results are computed using COMSOL Multiphysics software [58] (unless stated otherwise) applying the “*SWEs interface*” which allows to implement the source terms and the extra terms containing the Λ function. To solve the equations, this interface uses the finite element method (FE), which employs nodal discontinuous Lagrange functions with constant element order. For cross-validation and the possibility of using inversion computational tools (such as adjoint models, optimization procedures, etc), the system (4.21) is also implemented into the DassFlow open-source software [59], which employs finite volume (FV) schemes (both first and second order), see [60,61] for the Newtonian case. For the present Herschel–Bulkley case, the first order FV scheme has been enriched; details are presented in Appendix A. Experimental data is extracted from the literature using the WebPlotDigitizer open-source software [62] with an estimated error margin of less than 5%. For all numerical simulations presented hereafter, the coefficient of slipperiness C is set to zero, unless stated otherwise.

5.1 Dam-break flows on an inclined surface

The dam-break experiment presented in [63] is considered here for validation of the mathematical model and numerical simulations. This experiment involves the sudden release of fixed volumes of a viscoplastic fluid (Carbopol ultrez 10 at a mass concentration of 0.15%) down a channel of length 3.5 m and width 0.3 m, inclined at some angle θ , as shown in Fig. 3.

The fluid is initially locked in a reservoir of length 0.5 m, set at the top of the flume before it is released

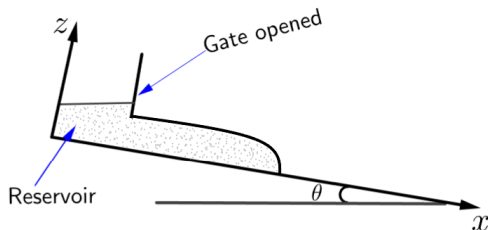


Figure 3: Side-view sketch of a dam-break problem.

suddenly by opening the lock gate. The initial height is described by

$$h(x) = \begin{cases} 0.12 + (x - 0.25)\tan\theta & \text{for } x \leq 0.5, \\ 0 & \text{otherwise.} \end{cases} \quad (5.1)$$

Recall that depth-averaged models like the present SW system are not able to accurately describe flow dynamics at the very start of dam-break, in particular due to the long-wave assumption ($\varepsilon = \frac{H^*}{L^*}$ small). In practice, the long wave assumption can be considered valid if ε lower than ≈ 0.3 , see e.g. [51]. This assumption

is not satisfied at the very early stages of dam-break. However, this assumption is satisfied everywhere else and very quickly at the dam location. In the present dam-break experiment, $(h_{reservoir}/l_{reservoir})=0.24$, therefore satisfying a reasonable ratio.

The fluid is of density $\rho = 1000 \text{ kg m}^{-3}$ and its rheological properties given by Eq. (5.2):

$$(K, n, \tau_c) = (26 \text{ Pa s}^n, 0.33, 33 \text{ Pa}) \quad (5.2)$$

A wall condition is used on all boundaries. For further details on the experimental procedure and uncertainties involved, see [63].

Firstly, to ensure convergence of results, a grid independence study is performed. Fig. 4 shows the fluid height and the corresponding mean velocity for 4 different meshes: coarse (1500 elements), medium (3000 elements), fine (5000 elements), and extremely fine (50000 elements). The extremely fine mesh is assumed to represent the exact solution. The study is performed considering Regime A on an inclination $\theta = 15^\circ$. As shown in Fig. 4, all four meshes show similar results, with a slight difference appearing around the maximum of the mean velocity. The medium mesh is chosen for the rest of the simulations in this subsection since both the computational time and accuracy of the results are satisfactory.

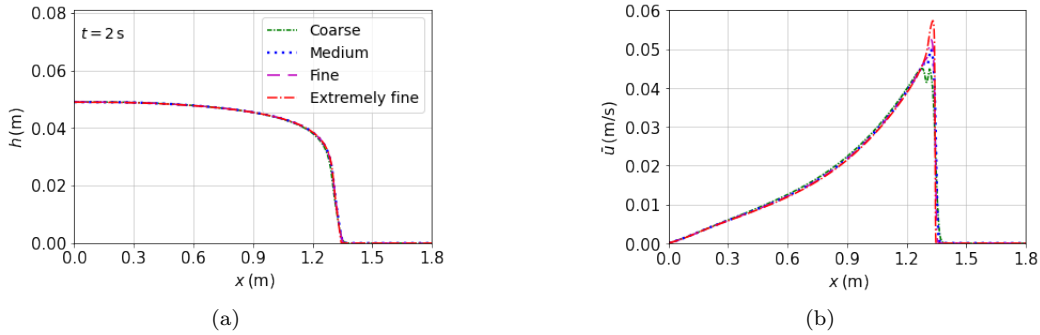


Figure 4: Mesh convergence study: (a) fluid height and (b) the corresponding mean velocity for different mesh sizes at $t = 2 \text{ s}$.

Next, numerical simulations are compared with experiments for inclination $\theta = 15^\circ$ and $\theta = 25^\circ$, respectively, see Fig. 5. The front positions are plotted against time for both Regimes, A and B. Numerical results of a similar viscoplastic model (one-layer model) presented in [47] are also plotted for cross-validation. The present results are found to be in better agreement with experimental results than with solutions obtained by [47]. Notably, both regime models compare fairly well with the experiments and the difference between the two solutions is small. The slight difference between the present regime models and the experimental data, especially for longer times (see Fig. 5 (b)) can be attributed to the sidewall friction effects reported in the experiment [63], which are not accounted for in the present model.

To investigate the two regimes further, the time evolution of the elevation profile for the two flow regimes is shown in Fig. 6 for the two slope angles. The maximum relative difference between the two regimes is calculated by $\frac{|x_{fB} - x_{fA}|}{|x_{fA}|}$, where subscripts A and B denote the two regimes, respectively. A difference of about 7.5% for $\theta = 15^\circ$ and 2.5% for $\theta = 25^\circ$, is observed between the two regimes at the front zone, where there is a sharp change of the fluid slope $\frac{\partial h}{\partial x}$. This difference, however, diminishes everywhere else within the flow profile. The front zone is usually determined by the balance between the gravitational acceleration $g \frac{\partial h}{\partial x}$

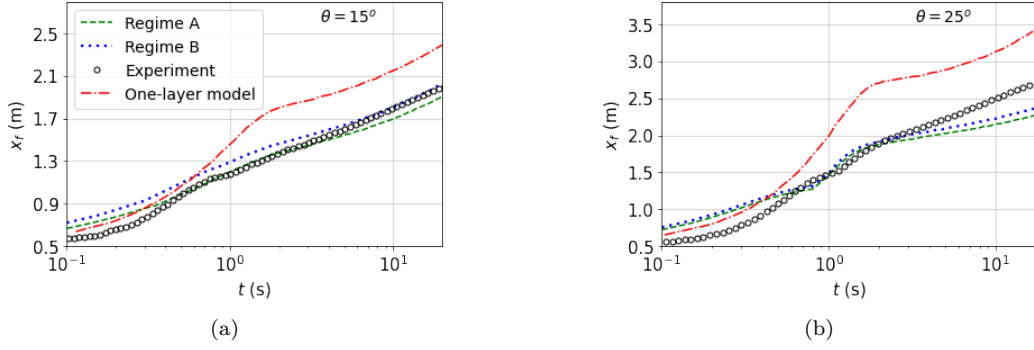


Figure 5: Comparing Regime A and B with experiments [63] and with solutions of the one-layer model presented in [47]: front positions x_f varying with time t in semilog scale, for (a) $\theta = 15^\circ$ and (b) $\theta = 25^\circ$, respectively.

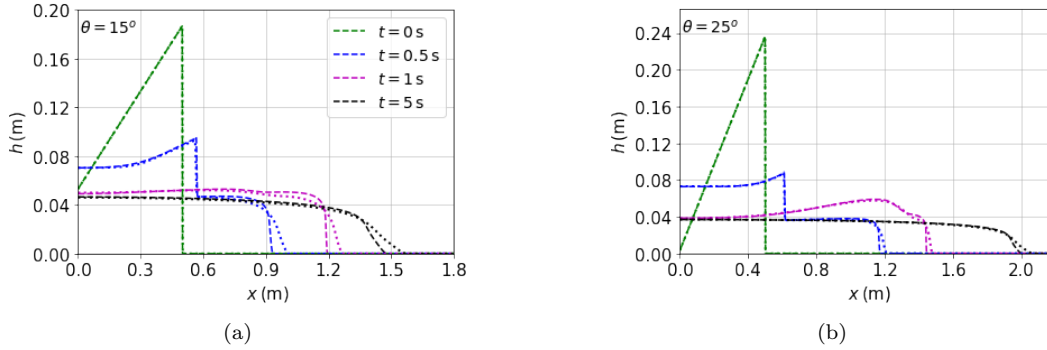


Figure 6: Comparing Regime A (dashed line) and Regime B (dotted line) for two different inclination angles.

and the basal shear stress τ_b , with the slope $\frac{\partial h}{\partial x}$ having the dominant effects. The difference between the two regimes is larger for $\theta = 15^\circ$ than for $\theta = 25^\circ$, since the height gradient $\frac{\partial h}{\partial x}$ is larger for $\theta = 15^\circ$ than for $\theta = 25^\circ$. This shows that the difference between the two regimes occurs in areas with sharp changes of the fluid local slopes and increases when the height gradient increases.

5.2 Steady flow over a bump

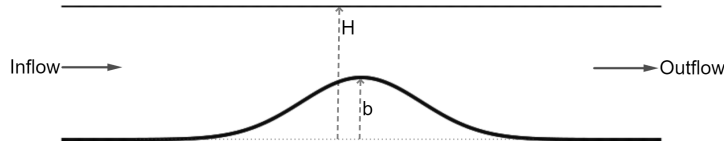


Figure 7: Flow geometry on a flat topography with a bump at the center

To investigate the two regimes further, a steady state flow on an inclined topography ($\theta = 15^\circ$) with a bump at the center is considered, as shown in Fig. 7. The topography given by $b(x) = b_0 e^{-0.15(2x-L)^2}$, where

b_o is the height of the bump, is set on a domain of length $L = 10$ m and width 1 m. To vary the mean-slope of the topography, two different heights of the bump are considered for analysis: $b_o = 0.1$ m and 0.3 m, respectively. A discharge $q = 0.12 \text{ m}^2 \text{ s}^{-1}$ is imposed at the upstream boundary, and a fluid depth of 0.5 m imposed at the outflow. The fluid density used is $\rho = 1000 \text{ kg m}^{-3}$ together with the rheological parameters given by Eq. (5.2). To ensure the convergence of the solution, a medium mesh, as described in the previous section, is chosen here for discretization with $\Delta t = 0.05$ s. Simulations were run over time until a steady state was reached at about $t = 20$ s, with a steady-state tolerance of about 10^{-7} . The tolerance is obtained by calculating the relative error between solutions of two consecutive time steps, which should satisfy the condition $\frac{|h^{n+1} - h^n|}{|h^n|} < 10^{-3}$. Fig. 8 compares the steady-state solutions (h, \bar{u}) of the two regimes, Regime

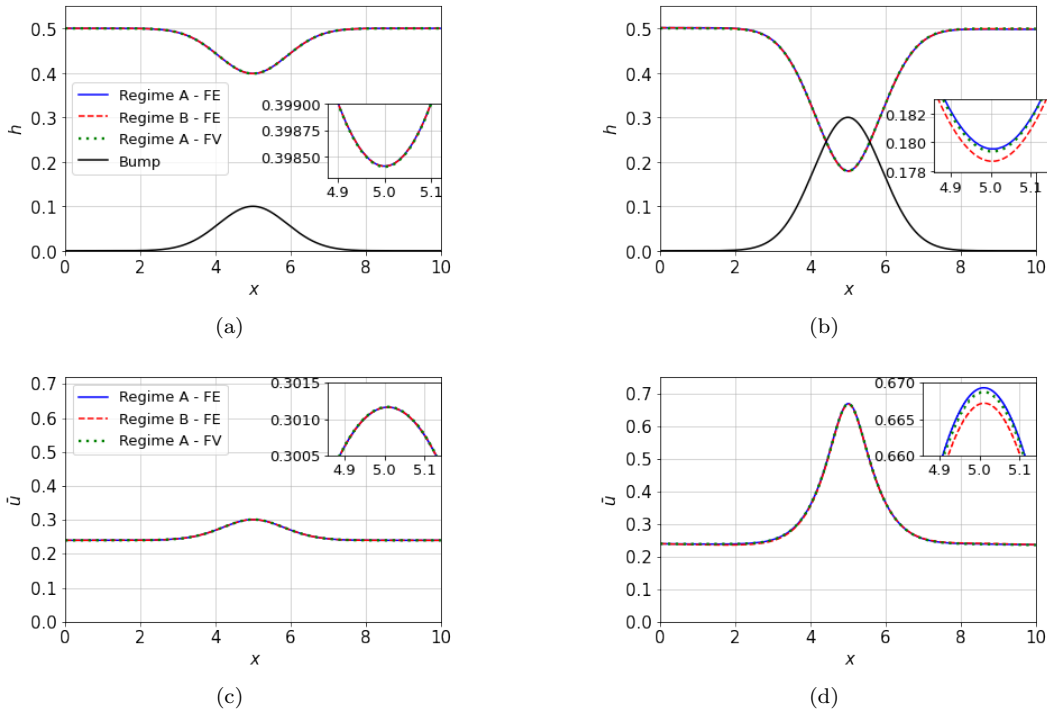


Figure 8: Comparing Regime A and B for two different heights of the bump: $b_o = 0.1$ m and 0.3 m, respectively.

A and B, for the two values of the bump height. Results for Regime A from both COMSOL Multiphysics and DassFlow softwares are plotted for cross-comparison, which shows excellent agreement. The difference between the two regimes, however, is negligible within the state variables (h, \bar{u}) for the two cases of the bump height. Nevertheless, on zooming out, a slight difference of about 0.5% between the two regimes is observed around the top region of the taller bump, where the local slope is sharp. This disparity, however, is negligible everywhere else. Note that the difference between the two regimes is calculated by $\frac{|h_B - h_A|}{|h_A|} \times 100$, where the subscripts A and B denote the two regimes, respectively.

To study the difference between the two flow regimes further, the gravity term defined in Section 3.2 is normalized as

$$\frac{\Lambda}{\lambda} = \begin{cases} 1 & \text{for regime A,} \\ 1 - \frac{\delta}{\lambda} \partial_x H & \text{for regime B,} \end{cases} \quad (5.3)$$

from which a regime correction criterion differentiating the two regimes can be defined as $\frac{\delta}{\lambda} \partial_x H$. We recall

that in physical dimensions $\frac{\delta}{\lambda} = \cot\theta$ and $\lambda = \frac{\rho g}{K}$.

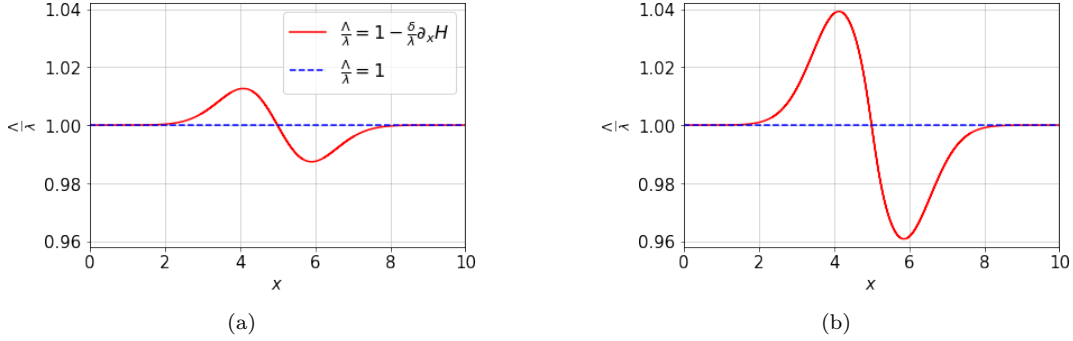


Figure 9: Comparing the normalized gravity term $\frac{\delta}{\lambda}$ for Regime A and B for two different heights of the bump.

By plotting Eq. 5.3, based on the simulation of the present case, the difference brought about by the correction criterion is now visible around the bump area ($2\text{ m} < x < 8\text{ m}$) and negligible everywhere else, see Fig. 9. This difference is maximum at the top region of the bump around $4\text{ m} < x < 6\text{ m}$, on both upstream and downstream of the bump, where there is a sharp change of the slope. This shows that the correction criterion ($\frac{\delta}{\lambda} \partial_x H$) increases as the height gradient increases due to the increase of the height of the bump, thereby increasing the difference between the two regimes. The 1.2% and 4% disparity observed in Fig. 9 (a) and (b), respectively, however, have an insignificant effect on the state variables of a steady-state flow, as observed earlier in Fig. 8. This suggests that the corrective term in Regime B improves solutions in areas with a very sharp change of slope, otherwise can be neglected for steady state flows.

5.3 2D dam-breach

To demonstrate the applicability of the present model to 3D flows, we consider a partial dam-breach problem studied in [64–66]. The setup is on a 200 m by 200 m domain with a sluice gate of thickness 10 m situated at the center as shown in Fig. 10. The gates are nonsymmetrical to demonstrate a general case for geophysical and/or engineering applications. The initial upstream and downstream fluid levels are 10 m and 5 m, respectively. Note that this case is investigated using Regime B, since Regime A is only valid for $\theta > 0^\circ$, as remarked previously.

For comparison with the results in the literature, the fluid rheological information used is given by Eq. (5.4). A coarse mesh of 60×60 structured elements is considered. Note that the very coarse 40×40 mesh cells used in [64, 65] do not provide sufficiently converged numerical solutions for the present simulations. A wall condition is used on all boundaries.

$$(K, n, \tau_c) = (0.001 \text{ Pa}\cdot\text{s}, 1, 0 \text{ Pa}) \quad (5.4)$$

The fluid is initially at rest before the gate is opened instantaneously to produce a bore-like wave that moves downstream (right) and a negative wave that tends to move upstream (left), see Fig. 11. The numerical

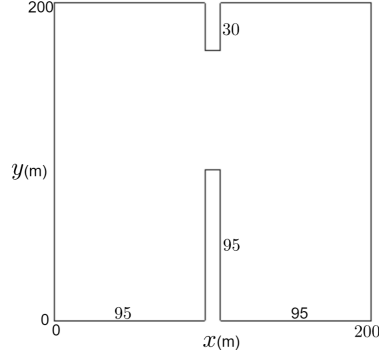


Figure 10: Dam-breach flow configuration (top-view).

simulations shown are for $t = 7.2$ s, before the positive wave reaches the downstream wall. Fig. 11 (a) and (b) show the free-surface profile and velocity field from the literature [64–66] while (c) and (d), show the corresponding results of the present model (4.21). The present results are shown to compare fairly well with those obtained by [64–66]. The velocity vectors point in the direction of the propagating wave past the gate.

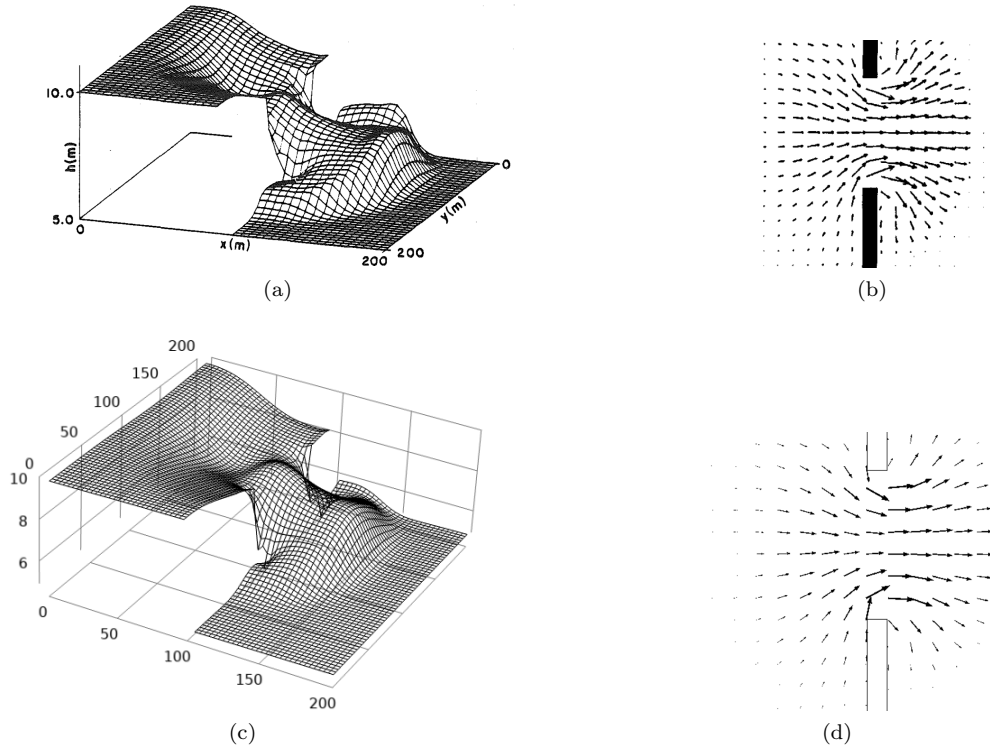


Figure 11: Dam-breach problem. Newtonian case: comparing the (a) fluid surface and (b) velocity vector from [64, 65] with (c) - (d) the present simulations, respectively.

To consider a viscoplastic case, the rheological parameters given by Eq. (5.5) are considered, and the mesh size increased to 100×100 elements to achieve the convergence of results.

$$(K, n, \tau_c) = (0.1, \text{Pa s}, 0.33, 33 \text{ Pa}) \quad (5.5)$$

As seen in the Newtonian case above, a bore-like wave propagating downstream is observed; see Fig. 12

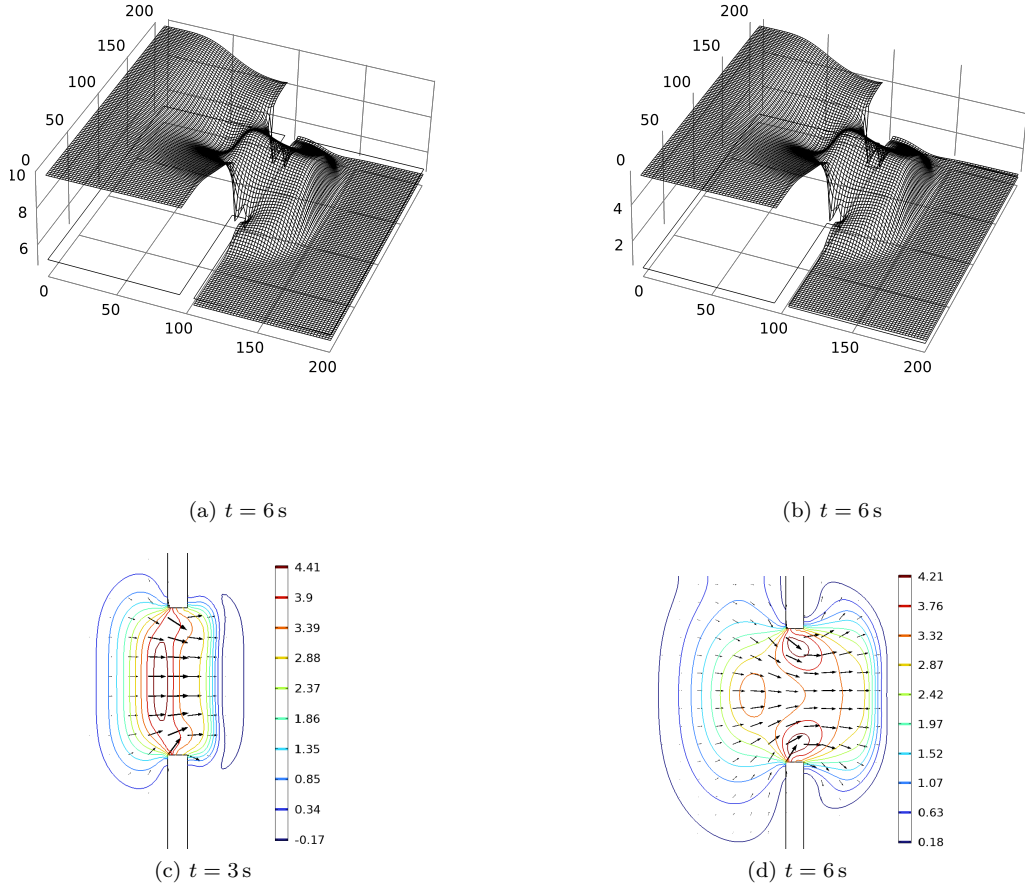


Figure 12: Dam-break problem. Herschel-Bulkley case showing (a) the fluid depth profile and the corresponding (b) yield surface at $t = 6$ s, mean velocity field at (c) $t = 3$ s and (d) $t = 6$ s, respectively.

(a). The corresponding yield surface is also plotted in Fig. 12 (b), which shows the evolution of the sheared thickness. Further, contour plots of the velocity field at $t = 3$ s and $t = 6$ s are shown in Fig. 12 (c) and (d), respectively. The arrows of the velocity field point towards the direction propagated by the upstream wave. At $t = 3$ s, the fluid is observed to force its way out through the gate before it spreads in all directions, as seen for $t = 6$ s. The mean velocity is maximum in the gate region where the flow passage is minimum (and therefore the velocity must increase there - the conservation of momentum). The velocity then decreases on either side of it.

5.4 Dam-break flows over a slippery bed

To test the robustness of the present model (4.21) to simulate slip conditions, the coefficient of slipperiness C is varied to investigate three basal slip cases: a non-slip ($C = 0$), a pure slip ($C = 10$ to represent $C \rightarrow \infty$),

and a transition between the two cases ($C = 0.5$), see [22]. The dam-break problem described in Subsection 5.1 is used here for the simulations. However, a set of different rheological values (sourced from [67]) of a relatively more viscous flow regime (given by Eq 5.6) is used here for analysis. The study is performed considering Regime A on a shallow slope $\theta = 6^\circ$.

$$(K, n, \tau_c) = (50 \text{ Pa}\cdot\text{s}, 0.5, 40 \text{ Pa}) \quad (5.6)$$

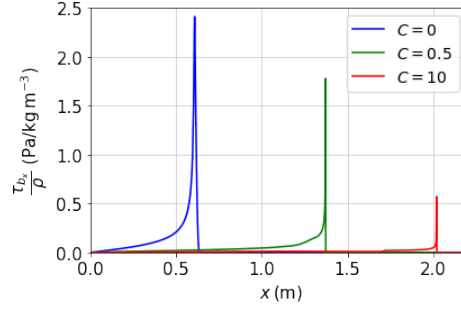


Figure 13: Variation of the basal slipperiness. Herschel-Bulkley case showing the basal shear stress profiles for three different values of the slip coefficient at $t = 1$ s.

The basal shear stress (frictional resistance) between the fluid and the bed is observed to reduce as the slipperiness coefficient increases, see Fig. 13. This implies that the fluid encounters less resistance from the basal topography as the slip coefficient increases, hence, reducing the shear rate. Consequently, the sliding of the fluid over the bed increases, and the fluid tends to spread faster.

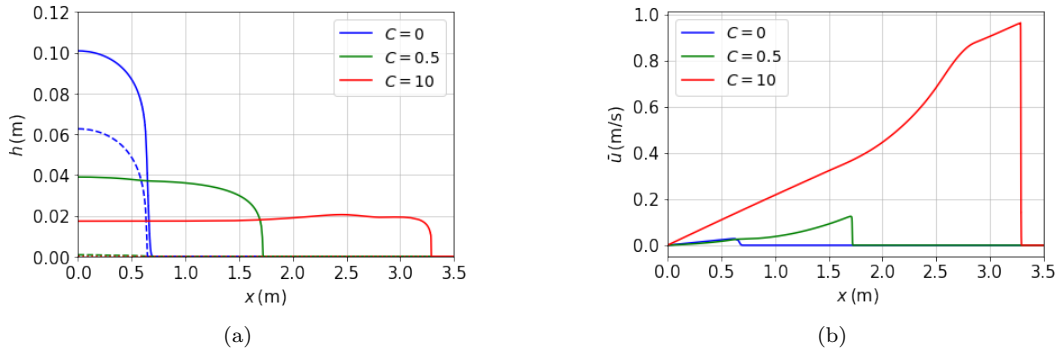


Figure 14: Variation of the basal slipperiness. Herschel-Bulkley case showing the evolution of (a) fluid depth (solid), yield surface (dashed), and (b) mean velocity for three different values of the slip coefficient at $t = 2$ s, respectively.

When the coefficient of slipperiness is increased, the front position of the free-surface profile is observed to advance faster and the corresponding mean velocity observed to increase, see Fig. 14. This is due to the decrease in frictional resistance. Furthermore, the plug thickness is observed to increase with the increase in the basal slip coefficient, see Fig. 14 (a). This implies that the shear rate of the fluid vanishes as the basal slipperiness approaches infinity, hence a plug flow. Conclusively, the results presented show that basal properties (e.g., basal slipperiness) have an influence on the dynamics of fluid flows, hence, it is important to have a model that accounts for them.

6 Conclusion

This paper presents the derivations of thin-layer flow models (lubrication and shallow water equations), valid for 3D multi-regime flows of viscoplastic Herschel–Bulkley fluids over non-flat inclined topographies with basal slipperiness. Upon considering a free-surface flow with varying basal conditions, these models are derived from the Navier–Stokes equations through an asymptotic analysis and the multi-regime approach, which allows to model different flow regimes originating from the variation of the mean-slope, basal elevation, and/or the basal boundary conditions. Two flow regimes (Regime A, the basic/classical one, and Regime B, the enriched one) corresponding to different balances between shear and pressure forces are defined and investigated. Flow models corresponding to these regimes are calculated. Classical reference solutions in the literature are recovered by considering particular cases on flat topographies.

Numerical solutions of the shallow water equations are obtained using two simulation softwares based on the finite element method (for COMSOL Multiphysics [58]) and finite volume method (for DassFlow [59], an open-source software), for cross-validation. The solutions of the two regime models are compared with experiments and related results from the literature, and are found to be in good agreement. The difference between the two regimes, however, is observed to occur in areas with sharp changes of the local slopes within unsteady flows, otherwise, it is negligible everywhere else. Flow models for Regime A, which are mathematically less complex to solve than those for Regime B, can therefore be used reliably to simulate free-surface flows of Herschel–Bulkley fluids, unless the mean-slope variation is very sharp.

Moreover, basal perturbations in topography elevation and basal slipperiness are observed to impact fluid flow dynamics, hence, it is important to include them in the model. In addition, the present flow models derived here are shown to be able to simulate 3D complex flows presenting Herschel-Bulkley rheology like lava and mud flows, which is the next step of the present study.

Declaration of competing interest

The authors declare that they have no known competing financial interests or personal relationships that could have appeared to influence the work reported in this paper

Acknowledgments & authors' contributions

The authors would like to thank the Royal Society of New Zealand, through the Marsden grant UOC1802, for providing funds to do this research towards the completion of the first author's PhD studies. The authors would like to thank two anonymous for providing insightful comments and suggestions too.

The first author derived the equations and built up the computational methods from the previous studies, which are mentioned here, under the guidance of the second (corresponding) author. Software implementation was achieved under the supervision of the second author for DassFlow2D (which was originally considering the Newtonian case only) and the third author for COMSOL Multiphysics. All authors participated in the validation and analysis of the results. The second and third authors obtained funding for this project.

The second author would like to warmly acknowledge Prof. J-P Vila from INSA - Mathematics Institute of Toulouse for having introduced these model derivation techniques, and G. Chambon for providing us with his Habilitation thesis.

References

- [1] C Ancey. Plasticity and geophysical flows: a review. *Journal of Non-Newtonian Fluid Mechanics*, 142:4–35, 2007.
- [2] NJ Balmforth, IA Frigaard, and G Ovarlez. Yielding to stress: recent developments in viscoplastic fluid mechanics. *Annual Review of Fluid Mechanics*, 46:121–146, 2014.
- [3] I Frigaard. Simple yield stress fluids. *Current Opinion in Colloid & Interface Science*, 43:80–93, 2019.
- [4] RB Bird, GC Dai, and BJ Yarusso. The rheology and flow of viscoplastic materials. *Reviews in Chemical Engineering*, 1(1):1–70, 1983.
- [5] N Roussel and P Coussot. "fifty-cent rheometer" for yield stress measurements: from slump to spreading flow. *Journal of Rheology*, 49(3):705–718, 2005.
- [6] P Saramito and A Wachs. Progress in numerical simulation of yield stress fluid flows. *Rheologica Acta*, 56:211–230, 2017.
- [7] B Merz, C Kuhlicke, M Kunz, M Pittore, A Babeyko, DN Bresch, DIV Domeisen, F Feser, I Koszalka, and H Kreibich. Impact forecasting to support emergency management of natural hazards. *Reviews of Geophysics*, 58(4):e2020RG000704, 2020.
- [8] B Cordonnier, E Lev, and F Garel. Benchmarking lava-flow models. *Geological Society, London, Special Publications*, 426(1):425–445, 2016.
- [9] JM Saville, EM Hinton, and HE Huppert. Predicting safe regions within lava flows over topography. *Journal of Geophysical Research: Solid Earth*, 127(9):e2022JB024167, 2022.
- [10] J-M Piau. Flow of a yield stress fluid in a long domain. Application to flow on an inclined plane. *Journal of Rheology*, 40:711–723, 1996.
- [11] NJ Balmforth and RV Craster. A consistent thin-layer theory for Bingham plastics. *Journal of Non-Newtonian Fluid Mechanics*, 84:65–81, 1999.
- [12] MM Denn and D Bonn. Issues in the flow of yield-stress liquids. *Rheologica Acta*, 50:307–315, 2011.
- [13] P Freydier, G Chambon, and M Naaim. Experimental characterization of velocity fields within the front of viscoplastic surges down an incline. *Journal of Non-Newtonian Fluid Mechanics*, 240:56–69, 2017.
- [14] EC Bingham. *Fluidity and plasticity*. McGraw-Hill, 1922.
- [15] WH Herschel and R Bulkeley. Measurement of consistency of rubber-benzene solutions. *Kolloid-zeitschrift*, 39:291–298, 1926.
- [16] NJ Balmforth, RV Craster, AC Rust, and R Sassi. Viscoplastic flow over an inclined surface. *Journal of Non-Newtonian Fluid Mechanics*, 139:103–127, 2006.
- [17] C Ancey and S Cochard. The dam-break problem for Herschel–Bulkeley viscoplastic fluids down steep flumes. *Journal of Non-Newtonian Fluid Mechanics*, 158:18–35, 2009.

- [18] IR Ionescu. Viscoplastic shallow flow equations with topography. *Journal of Non-Newtonian Fluid Mechanics*, 193:116–128, 2013.
- [19] G Chambon, A Ghemmour, and M Naaïm. Experimental investigation of viscoplastic free-surface flows in a steady uniform regime. *Journal of Fluid Mechanics*, 754:332–364, 2014.
- [20] P Coussot. Yield stress fluid flows: A review of experimental data. *Journal of Non-Newtonian Fluid Mechanics*, 211:31–49, 2014.
- [21] N Bernabeu, P Saramito, and C Smutek. Modelling lava flow advance using a shallow-depth approximation for three-dimensional cooling of viscoplastic flows. *Geological Society, London, Special Publications*, 426:409–423, 2016.
- [22] M Boutounet, J Monnier, and J-P Vila. Multi-regime shallow free surface laminar flow models for quasi-Newtonian fluids. *European Journal of Mechanics-B/Fluids*, 55:182–206, 2016.
- [23] CB Vreugdenhil. *Numerical methods for shallow water flow*, volume 13. Springer Science & Business Media, 1994.
- [24] H-C Chang and EA Demekhin. Complex wave dynamics on thin films. 2002.
- [25] RM Iverson. Debris flows: behaviour and hazard assessment. *Geology Today*, 30(1):15–20, 2014.
- [26] P Papale. Rational volcanic hazard forecasts and the use of volcanic alert levels. *Journal of Applied Volcanology*, 6(1):1–13, 2017.
- [27] KF Liu and CC Mei. Slow spreading of a sheet of Bingham fluid on an inclined plane. *Journal of Fluid Mechanics*, 207:505–529, 1989.
- [28] X Huang and MH Garcia. A Herschel–Bulkley model for mud flow down a slope. *Journal of Fluid Mechanics*, 374:305–333, 1998.
- [29] NJ Balmforth, RV Craster, P Perona, AC Rust, and R Sassi. Viscoplastic dam breaks and the Bostwick consistometer. *Journal of Non-Newtonian Fluid Mechanics*, 142(1-3):63–78, 2007.
- [30] N Bernabeu, P Saramito, and C Smutek. Numerical modelling of non-Newtonian viscoplastic flows: Part II. viscoplastic fluids and general tridimensional topographies. *International Journal of Numerical Analysis and Modeling*, 11:213–228, 2014.
- [31] Y Liu, NJ Balmforth, S Hormozi, and DR Hewitt. Two-dimensional viscoplastic dambreaks. *Journal of Non-Newtonian Fluid Mechanics*, 238:65–79, 2016.
- [32] D Benney. Long waves on liquid films. *Journal of Mathematics and Physics*, 45:150–155, 1966.
- [33] KF Liu and CC Mei. Approximate equations for the slow spreading of a thin sheet of Bingham plastic fluid. *Physics of Fluids A: Fluid Dynamics*, 2(1):30–36, 1990.
- [34] A Pumir, P Manneville, and Y Pomeau. On solitary waves running down an inclined plane. *Journal of Fluid Mechanics*, 135:27–50, 1983.
- [35] C Ruyer-Quil and P Manneville. Improved modeling of flows down inclined planes. *The European Physical Journal B-Condensed Matter and Complex Systems*, 15:357–369, 2000.

- [36] ED Fernández-Nieto, P Noble, and J-P Vila. Shallow water equations for non-Newtonian fluids. *Journal of Non-Newtonian Fluid Mechanics*, 165:712–732, 2010.
- [37] P Noble and J-P Vila. Thin power-law film flow down an inclined plane: consistent shallow water models and stability under large-scale perturbations. *Journal of Fluid Mechanics*, 735:29–60, 2013.
- [38] AJC De Saint-Venant. Theorie du mouvement non-permanent des eaux, avec application aux crues des rivieres et a l’introduction des marees dans leur lit. *Comptes rendus des Seances de l’Academie des Sciences Paris*, 73(147-154):237–240, 1871.
- [39] C Ruyer-Quil and P Manneville. Modeling film flows down inclined planes. *The European Physical Journal B-Condensed Matter and Complex Systems*, 6:277–292, 1998.
- [40] J-F Gerbeau and B Perthame. *Derivation of viscous Saint-Venant system for laminar shallow water; numerical validation*. PhD thesis, INRIA, 2000.
- [41] R Usha and B Uma. Modeling of stationary waves on a thin viscous film down an inclined plane at high Reynolds numbers and moderate Weber numbers using energy integral method. *Physics of Fluids*, 16(7):2679–2696, 2004.
- [42] GL Richard, C Ruyer-Quil, and J-P Vila. A three-equation model for thin films down an inclined plane. *Journal of Fluid Mechanics*, 804:162–200, 2016.
- [43] D Bresch, ED Fernandez-Nieto, IR Ionescu, and P Vigneaux. Augmented Lagrangian method and compressible viscoplastic flows: applications to shallow dense avalanches. *New Directions in Mathematical Fluid Mechanics*, pages 57–89, 2009.
- [44] D Denisenko, G Richard, and G Chambon. A consistent three-equation shallow-flow model for Bingham fluids. *Journal of Non-Newtonian Fluid Mechanics*, 321:105111, 2023.
- [45] C Acary-Robert, ED Fernández-Nieto, G Narbona-Reina, and P Vigneaux. A well-balanced finite volume-augmented lagrangian method for an integrated Herschel-Bulkley model. *Journal of Scientific Computing*, 53:608–641, 2012.
- [46] G Chambon. *Quelques contributions à la modélisation des écoulements à surface libre de fluides complexes*. PhD thesis, HDR en Sciences de la Planète et de l’Environnement, Université de Grenoble I, 2014.
- [47] ED Fernández-Nieto, J Garres-Díaz, and P Vigneaux. Multilayer models for hydrostatic Herschel-Bulkley viscoplastic flows. *Computers & Mathematics with Applications*, 139:99–117, 2023.
- [48] F Bouchut and S Boyaval. Unified derivation of thin-layer reduced models for shallow free-surface gravity flows of viscous fluids. *European Journal of Mechanics-B/Fluids*, 55:116–131, 2016.
- [49] J Weertman. On the sliding of glaciers. *Journal of Glaciology*, 3(21):33–38, 1957.
- [50] G Hulme. The interpretation of lava flow morphology. *Geophysical Journal International*, 39(2):361–383, 1974.
- [51] RW Griffiths. The dynamics of lava flows. *Annual Review of Fluid Mechanics*, 32:477–518, 2000.

- [52] H Blatt, R Tracy, and B Owens. *Petrology: igneous, sedimentary, and metamorphic*. Macmillan, 2006.
- [53] AJL Harris and JS Allen III. One-, two- and three-phase viscosity treatments for basaltic lava flows. *Journal of Geophysical Research: Solid Earth*, 113, 2008.
- [54] MO Chevrel, H Pinkerton, and AJL Harris. Measuring the viscosity of lava in the field: a review. *Earth-Science Reviews*, 196:102852, 2019.
- [55] N Martin and J Monnier. Inverse rheometry and basal properties inference for pseudoplastic geophysical flows. *European Journal of Mechanics-B/Fluids*, 50:110–126, 2015.
- [56] GB Whitham. The effects of hydraulic resistance in the dam-break problem. *Proceedings of the Royal Society of London. Series A. Mathematical and Physical Sciences*, 227(1170):399–407, 1955.
- [57] AJ Hogg and D Pritchard. The effects of hydraulic resistance on dam-break and other shallow inertial flows. *Journal of Fluid Mechanics*, 501:179–212, 2004.
- [58] COMSOL Multiphysics and CMHT Module. COMSOL Multiphysics user’s guide. *Version: COMSOL Multiphysics*, 3, 2014.
- [59] J Monnier, K Larnier, L Pujol, F Couderc, and P-A et al. Garambois. Dassflow, open-source computational software. <https://www.math.univ-toulouse.fr/DassFlow>.
- [60] J Monnier, F Couderc, D Dartus, K Larnier, R Madec, and J-P Vila. Inverse algorithms for 2D shallow water equations in presence of wet dry fronts: Application to flood plain dynamics. *Advances in Water Resources*, 97:11–24, 2016.
- [61] L Pujol, P-A Garambois, and J Monnier. Multi-dimensional hydrological-hydraulic model with variational data assimilation for river networks and floodplains. *Geoscientific Model Development*, 15:6085–6113, 2022.
- [62] A Rohatgi. Webplotdigitizer user manual version 3.4. <http://arohatgi.info/WebPlotDigitizer/app>, pages 1–18, 2014.
- [63] C Ancey, N Andreini, and G Epely-Chauvin. Viscoplastic dambreak waves: Review of simple computational approaches and comparison with experiments. *Advances in Water Resources*, 48:79–91, 2012.
- [64] RJ Fennema and MH Chaudhry. Explicit methods for 2D transient free surface flows. *Journal of Hydraulic Engineering*, 116(8):1013–1034, 1990.
- [65] CG Mingham and DM Causon. High-resolution finite-volume method for shallow water flows. *Journal of Hydraulic Engineering*, 124(6):605–614, 1998.
- [66] S-J Liang, J-H Tang, and M-S Wu. Solution of shallow-water equations using least-squares finite element method. *Acta Mechanica Sinica*, 24:523–532, 2008.
- [67] DK Muchiri, JN Hewett, M Sellier, M Moyers-Gonzalez, and J Monnier. Numerical simulations of dam-break flows of viscoplastic fluids via shallow water equations. Submitted <https://doi.org/10.21203/rs.3.rs-3103251/v1>, 2024.
- [68] EF Toro. *Riemann solvers and numerical methods for fluid dynamics: a practical introduction*. Springer Science & Business Media, 2013.

- [69] Fr Couderc, J Monnier, J-P Vila, K Larnier, R Madec, and D Dartus. Robust finite volume schemes for 2D shallow water models. application to flood plain dynamics. *HAL-01133594*, 2015.
- [70] Q Liang and F Marche. Numerical resolution of well-balanced shallow water equations with complex source terms. *Advances in Water Resources*, 32:873–884, 2009.
- [71] E Audusse, F Bouchut, M Bristeau, R Klein, and B Perthame. A fast and stable well-balanced scheme with hydrostatic reconstruction for shallow water flows. *SIAM Journal on Scientific Computing*, 25:2050–2065, 2004.

A Appendix: Finite volume schemes

In this section, the solution procedure for the present shallow water equations is presented, following the work of [68, 69], see also [60, 61].

A.1 Conservative form

Firstly, the model is written in conservative form as

$$\partial_t \mathbf{U} + \partial_x \mathbf{F}(\mathbf{U}) + \partial_y \mathbf{G}(\mathbf{U}) = \mathbf{S}_g(\mathbf{U}) + \mathbf{S}_f(\mathbf{U}) \quad (\text{A.1})$$

where

$\mathbf{U} = \begin{bmatrix} h \\ h\bar{u} \\ h\bar{v} \end{bmatrix}$ is the vector of conserved variables,

$\mathbf{F}(\mathbf{U}) = \begin{bmatrix} h\bar{u} \\ h\bar{u}^2 + \frac{1}{2}gh^2\cos\theta + C_m \left[\frac{\rho g}{K} S_{\theta_x}\right]^{2m} h^{2m+3} \\ h\bar{u}\bar{v} + C_m \left[\frac{\rho g}{K} S_{\theta_x}\right]^{2m} h^{2m+3} \end{bmatrix}$ and $\mathbf{G}(\mathbf{U}) = \begin{bmatrix} h\bar{v} \\ h\bar{u}\bar{v} + C_m \left[\frac{\rho g}{K} S_{\theta_y}\right]^{2m} h^{2m+3} \\ h\bar{v}^2 + \frac{1}{2}gh^2\cos\theta + C_m \left[\frac{\rho g}{K} S_{\theta_y}\right]^{2m} h^{2m+3} \end{bmatrix}$

are the vectors of fluxes,

$\mathbf{S}_g(\mathbf{U}) = \begin{bmatrix} 0 \\ -gh \left(\cos\theta \frac{\partial b}{\partial x} - \sin\theta \right) \\ -gh \left(\cos\theta \frac{\partial b}{\partial y} - \sin\theta \right) \end{bmatrix}$ and $\mathbf{S}_f(\mathbf{U}) = \begin{bmatrix} 0 \\ -\frac{1}{\rho} \tau_{b_x} \\ -\frac{1}{\rho} \tau_{b_y} \end{bmatrix}$ are the vectors of sources. Basal shear

stress τ_b is given by (4.22).

Secondly, Godunov-type finite volume method is employed to solve the integrated form of the shallow water equations (A.1) which generally yields a semi-discretized equation of the form

$$\partial_t \mathbf{U} + \frac{1}{m_k} \sum_{e \in \partial k} m_e \hat{\mathbf{F}}_e(\mathbf{U}) = \mathbf{S}_g(\mathbf{U}) + \mathbf{S}_f(\mathbf{U}) \quad (\text{A.2})$$

where, following the notations defined in DassFlow [59]; Ω is the computational domain in 2D with N number of cells, k representing the cell index, m_k the area of the cell k , $m_{\partial k}$ perimeter of the cell k , k_e neighboring cell, e the cell edge, \mathbf{n}_e the unit normal vector to e , $n_{e,k}$ the unit normal vector to e pointing outward from k to k_e , m_e the length of the side e , and $\hat{\mathbf{F}}_e(\mathbf{U}) = \mathbf{F}_e(\mathbf{U}) n_{e_x} + \mathbf{G}_e(\mathbf{U}) n_{e_y}$ the intercell normal flux obtained by applying the rotational invariance property in Eq. (A.1), see [68]. This property enables us to reduce the

sum of a 2D problem to a 1D Riemann problem.

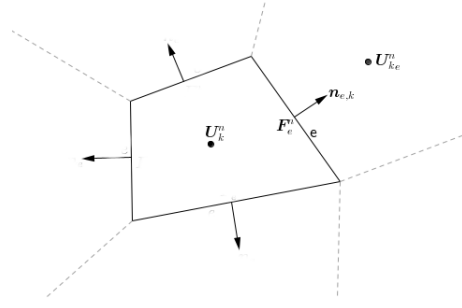


Figure 15: Finite volume cell k : showing the notations used for mesh discretization

A.2 Splitting method

To obtain a fully discretized system of Eq. (A.2), the splitting method is employed for the numerical treatment of fluxes and source terms. Splitting methods are commonly used to divide a long equation incorporating several time-dependent physical processes into simpler equations for individual physical process, which can be solved separately by numerical techniques [68, 70]. Incorporating the prediction and correction method, the splitting method here consists of two steps:

Step 1: Compute \tilde{U}^{n+1} solution of (A.2) without the friction term:

$$\partial_t \mathbf{U} + \frac{1}{m_k} \sum_{e \in \partial k} m_e \hat{\mathbf{F}}_e(\mathbf{U}) = \mathbf{S}_g(\mathbf{U}). \quad (\text{A.3})$$

Step 2: Given the predicted solution \tilde{U}^{n+1} , compute U_k^{n+1} solution of

$$\partial_t \mathbf{U} = \mathbf{S}_f(\mathbf{U}). \quad (\text{A.4})$$

It's noted that the solution \tilde{U}^{n+1} obtained in Step 1 is used to update the solution U_k^{n+1} obtained in Step 2. This procedure is described in the next subsection and detailed in [59]. Following these steps, the expected final scheme in general will take the form

$$U_k^{n+1} = \tilde{U}_k^{n+1} + \Delta t \mathbf{S}_f(\tilde{U}_k^{n+1}). \quad (\text{A.5})$$

It is evident from Eq. (A.1) and (A.5) that for a small fluid depth i.e., as $h \rightarrow 0$, the friction term becomes very large compared to other terms and can lead to numerical instability. In that sense, a small time step Δt can be chosen to maintain the stability, however, this can be computationally expensive. To overcome this drawback, a proper numerical treatment of the friction source term is required i.e., the friction source term can be treated implicitly while others are treated explicitly.

A.3 Interface fluxes and gravity source term discretization

Here, the fluxes and gravity source terms are treated explicitly, thus, integrating Eq. (A.3) in time, a

fully discrete system is obtained:

$$\tilde{\mathbf{U}}^{n+1} = \mathbf{U}_k^n - \frac{\Delta t}{m_k} \sum_{e \in \partial k} m_e \hat{\mathbf{F}}_e(\mathbf{U}^n) + \Delta t \mathbf{S}_g(\mathbf{U}^n) \quad (\text{A.6})$$

where, the subscript k represents the mesh cell index, superscript n the time level, $\Delta t = t^{n+1} - t^n$ the time step for $t \in [0, T]$, \mathbf{U}_k^n the approximation of \mathbf{U} at time t^n , and $\hat{\mathbf{F}}_e = \hat{\mathbf{F}}_{e,k} - \hat{\mathbf{F}}_{e,k_e}$ the numerical fluxes through the interfaces of cell k at time t^n . For clarity, it is worth noting that this can also be written as $\hat{\mathbf{F}}_e(\mathbf{U}^n) = \hat{\mathbf{F}}_e(\mathbf{U}_{e,k}^n) - \hat{\mathbf{F}}_e(\mathbf{U}_{e,k_e}^n)$ where $\mathbf{U}_{e,k}^n$ and \mathbf{U}_{e,k_e}^n are the vectors of the conservative variable on either side of edge e . The numerical scheme (A.6) is complete when numerical fluxes $\hat{\mathbf{F}}_e$ and gravity source term \mathbf{S}_g are reconstructed using finite volume methods developed in the literature, see e.g., [59, 68]. In this work, a Godunov-type scheme incorporated with a HLLC approximate Riemann solver is employed, as detailed in the DassFlow guide [59]. For the gravity source term, a well-balanced scheme developed in DassFlow (and references therein) which is stable for simulations involving wet-dry fronts is also adopted. To ensure positivity of the fluid depth and preservation of the fluid at rest property, Audusse et al. [71] considered a hydrostatic balance between the momentum components of the fluxes and gravity source term: $\frac{1}{2}g\nabla h^2 = -gh\nabla b$, and proposed a well balanced gravity source term scheme of the form $\mathbf{S}_g(\mathbf{U}^n) = -gh\nabla b \simeq \frac{1}{m_k} \sum_{e \in \partial k} m_e \frac{g}{2} \left[\left(h_{e,k}^n \right)^2 - \left(h_k^n \right)^2 \right] \mathbf{n}_{e,k}$, where the well-balanced discretization of the bed slope, if considering the x-direction, can be viewed as $\frac{\partial b}{\partial x} \simeq \frac{b_{e,k} - b_k}{\Delta x} \simeq \frac{h_k - h_{e,k}}{\Delta x}$, with $h_{e,k}$ representing the reconstructed hydrostatic water depth, at the left-hand side of the cell interface e . This is the first-order gravity source term scheme implemented in DassFlow for the Newtonian case.

In a similar approach, comparing with the Newtonian version in DassFlow [59] and Audusse et al. [71], a well-balanced discretization of the gravity source term $\mathbf{S}_g(\mathbf{U}) = -g(\cos\theta h\nabla b - h\sin\theta \mathbf{I})$ for the SWE model derived here is employed. For instance, considering the x -direction gravity term:

$$\begin{aligned} S_g &= -g \left(h \cos\theta \frac{\partial b}{\partial x} - h \sin\theta \right), \\ &\simeq -g \left[\left(\frac{h_{e,k} + h_k}{2} \right) \left(\frac{h_k - h_{e,k}}{\Delta x} \right) \cos\theta - \frac{h_{e,k} + h_k}{2} \sin\theta \right], \\ &\simeq \frac{g}{2\Delta x} \left[\left(h_{e,k}^2 - h_k^2 \right) \cos\theta + \Delta x \left(h_{e,k} + h_k \right) \sin\theta \right]. \end{aligned} \quad (\text{A.7})$$

Thus, in general, $\mathbf{S}_g(\mathbf{U}^n) = -gh^n(\cos\theta\nabla b - \sin\theta\mathbf{I}) \simeq \frac{1}{m_k} \sum_{e \in \partial k} m_e \frac{g}{2} \left[\left(\left(h_{e,k}^n \right)^2 - \left(h_k^n \right)^2 \right) \cos\theta + m_e \left(h_{e,k}^n + h_k^n \right) \sin\theta \right] \mathbf{n}_{e,k}$.

Substituting this into Eq. (A.6) yields

$$\tilde{\mathbf{U}}^{n+1} = \mathbf{U}_k^n - \frac{\Delta t}{m_k} \sum_{e \in \partial k} m_e \hat{\mathbf{F}}_e(\mathbf{U}^n) + \frac{\Delta t}{m_k} \sum_{e \in \partial k} m_e \frac{g}{2} \left[\left(\left(h_{e,k}^n \right)^2 - \left(h_k^n \right)^2 \right) \cos\theta + m_e \left(h_{e,k}^n + h_k^n \right) \sin\theta \right] \mathbf{n}_{e,k}. \quad (\text{A.8})$$

Using appropriate Riemann solver (HLLC), this scheme (for the fluxes and gravity term) together with other schemes (for other terms) are implemented in DassFlow for the non-Newtonian version.

Note: For further details of the hydrostatic reconstruction and numerical methods used, see [59, 71] and references therein.

A.4 Friction source term discretization

A stable implicit-scheme for the friction source term is required to avoid numerical instability as $h \rightarrow 0$. Using appropriate numerical methods, Eq. (A.4) can be solved conveniently to get a numerical scheme for the friction term. In an expanded form, this equation writes

$$\begin{aligned} \frac{\partial h}{\partial t} &= 0, \\ \frac{\partial \tilde{\mathbf{q}}}{\partial t} &= \mathbf{S}_f, \end{aligned} \quad (\text{A.9})$$

where $\mathbf{S}_f = -\frac{1}{\rho}\boldsymbol{\tau}_b$. It's noted that the component of the continuity equation is already zero i.e. $\frac{h^{n+1}-\tilde{h}^{n+1}}{\Delta t^n} = 0$, which implies that we only need to seek a solution for the non-zero component of the momentum equation. The fluid depth is thus updated as

$$h^{n+1} = \tilde{h}^{n+1}. \quad (\text{A.10})$$

where \tilde{h}^{n+1} is the fluid depth estimated at the previous time step in Step 1 above. Treating the friction source term implicitly, i.e., at time level t^{n+1} for all the state variables, the semi-implicit time step scheme writes

$$\frac{h^{n+1}\bar{\mathbf{u}}^{n+1} - \tilde{h}^{n+1}\tilde{\mathbf{u}}^{n+1}}{\Delta t^n} = -\frac{1}{\rho}\boldsymbol{\tau}_b^{n+1},$$

where \tilde{h}^{n+1} and $\tilde{\mathbf{u}}^{n+1}$ are the previous solutions at t^n obtained in **step 1** above. Further, this writes

$$\bar{\mathbf{u}}^{n+1} = \tilde{\mathbf{u}}^{n+1} - \frac{\Delta t^n}{\tilde{h}^{n+1}\rho}\boldsymbol{\tau}_b^{n+1}. \quad (\text{A.11})$$

recalling that the $\boldsymbol{\tau}_b$ expression reads

$$\boldsymbol{\tau}_b^{n+1} = \frac{K}{D} \left(\frac{K}{\rho g |S_\theta^n|} \right)^{m-1} \left(\frac{\tau_c}{\rho g \|S_\theta^n\|} + h_c^n \right) \mathbf{q}^{n+1}. \quad (\text{A.12})$$

Treating the flow rate term implicitly, Eq. (A.11) becomes

$$\bar{\mathbf{u}}^{n+1} = \tilde{\mathbf{u}}^{n+1} - \frac{\Delta t^n}{\rho \tilde{h}^{n+1}} \left[\frac{K}{D} \left(\frac{K}{\rho g |S_\theta^n|} \right)^{m-1} \left(\frac{\tau_c}{\rho g \|S_\theta^n\|} + h_c^n \right) \tilde{h}^{n+1} \tilde{\mathbf{u}}^{n+1} \right]. \quad (\text{A.13})$$

After rearrangement this results to

$$\bar{\mathbf{u}}^{n+1} = \tilde{\mathbf{u}}^{n+1} \left(\frac{\rho D}{\rho D + \Delta t^n K \left(\frac{K}{\rho g |S_\theta^n|} \right)^{m-1} \left[\frac{\tau_c}{\rho g \|S_\theta^n\|} + \tilde{h}_c^{n+1} \right]} \right). \quad (\text{A.14})$$

As $h \rightarrow 0$ then $\bar{\mathbf{u}}^{n+1} \rightarrow 0$, which implies that the fluid at rest property is preserved even at wet/dry fronts. This develops into the following full-implicit scheme:

$$\mathbf{U}_k^{n+1} = \begin{pmatrix} h^{n+1} \\ h^{n+1} \tilde{\mathbf{u}}^{n+1} \end{pmatrix} = \left[h^{n+1} \tilde{\mathbf{u}}^{n+1} \left(\frac{\tilde{h}^{n+1}}{\rho D + \Delta t^n K \left(\frac{K}{\rho g |S_\theta^n|} \right)^{m-1} \left[\frac{\tau_c}{\rho g |S_\theta^n|} + \tilde{h}_c^{n+1} \right]} \right)} \right]. \quad (\text{A.15})$$

Recall that the expressions for the critical depth h_c , the term S_θ , and the denominator D , are defined in Sec. 4. Conclusively, this scheme is also implemented in DassFlow together with other terms and results computed as presented in the previous section.

Remark: It is worth noting that only Regime A has been implemented in DassFlow. Further work needs to be done to implement Regime B.